Delft University of Technology

Document Version
Final published version

Licence
CC BY

Citation (APA)
Ooms, G., Pourquie, M., & Breugem, W. P. (2026). On the hydrodynamic stability of a viscous liquid jet enclosed in a narrow tube. *International Journal of Multiphase Flow*, *200*, Article 105712.
https://doi.org/10.1016/j.ijmultiphaseflow.2026.105712

International Journal of Multiphase Flow 200 (2026) 105712

Contents lists available at ScienceDirect

International Journal of Multiphase Flow

journal homepage: www.elsevier.com/locate/ijmulflow

Research Paper

On the hydrodynamic stability of a viscous liquid jet enclosed in a narrow tube

Gijs Ooms, Mathieu Pourquie, Wim-Paul Breugem *

J.M. Burgerscentrum, Faculty of Mechanical Engineering, Delft University of Technology, Mekelweg 2, 2628 CD Delft, The Netherlands

ARTICLE INFO

Dataset link: https://doi.org/10.4121/b28e9ad3-e1fc-499b-ab1c-9c78f18a75e1

Keywords:
Enclosed liquid jet
Core-annular flow
Hydrodynamic stability
Surface tension
Numerical simulation

ABSTRACT

We studied the hydrodynamic stability of a viscous liquid jet enclosed by a much less viscous fluid in a narrow vertical tube. In literature, this flow pattern is also known as perfect core-annular flow. The main objective is to unravel the competition between capillary and shear-driven instability mechanisms acting on the flow. The temporal stability of the flow was tested under laminar conditions for a small axisymmetric sinusoidal perturbation of the interface. To this purpose, numerical simulations were conducted using a finite-volume two-phase flow solver combined with a geometric Volume-of-Fluid method to capture the interface between the immiscible fluids. The simulation results are interpreted using linear stability theory for thin liquid jets in free space. The main conclusion is that perfect core-annular flow is hydrodynamically unstable, either through a capillary or a shear-driven instability. The competition between the two instability mechanisms is characterized by the Weber number based on the annular layer thickness, We_a. For $We_a \ll 1$, the flow is prone to a capillary instability, while for $We_a \gg 1$, the liquid jet may undergo atomization. Evidence is also found for a reduced growth rate of capillary instabilities in the presence of strong shear at high We_a.

1. Introduction

When two immiscible liquids are injected into a tube, one liquid in the center region (core) of the tube and the other one in the annular region (annulus), an enclosed jet develops. This flow pattern is also known as perfect core-annular flow (PCAF). Several experiments have been carried out in this way; see, for instance, Housz et al. (2017).

Joseph et al. (1997) wrote a review about core-annular flow. A more recent review with applications of core-annular flow is given by Xie et al. (2023). Li and Renardy (1999) made numerical simulations of the flow. Tripathi et al. (2017) paid much attention to the interfacial waves between the two liquids. Ooms et al. (2013) studied the levitation force in horizontal core-annular flow. Li (2023) made a systematic investigation of the influence of turbulence on the flow. Ooms and Poesio (2003) made a theoretical study of core-annular flow. Ooms and Pourquie (2024) investigated the influence of several physical parameters on the flow.

The core-annular flow can be in a vertical or horizontal tube; in this study it is vertical. Furthermore, we consider flow in a narrow tube for which surface tension is expected to have a major influence on the flow dynamics. Relatively little is known about this flow regime yet. Related studies have been performed by Guillot et al. (2007) and Rykner et al. (2024). Guillot et al. (2007) described the transition from a jet to drops as a transition from a convective to an absolute instability using lubrication theory for flow at a low Reynolds number and compared this with experiments. This has applications to two-phase flows in microfluidic devices. Rykner et al. (2024) evaluated the importance of inertia for the flow in a cylindrical capillary, using theory and Direct Numerical Simulation. This has an application to two-phase flows of water and water vapor in fuel cells.

The original motivation for the present study is related to theoretical work on core-annular flow from 1972 by the first author. Ooms (1972) performed a linear stability analysis of smooth core-annular flow of two ideal liquids, assuming a uniform base flow in both the core and the annulus. He concluded that the flow is hydrodynamically unstable. Furthermore, if the thickness of the annular layer is much smaller than the radius of the tube, the tube wall has a strong reducing effect on the growth rate of possible Rayleigh–Plateau and Kelvin–Helmholtz type of instabilities. In the present study, we extend this work by considering viscous fluids with a large viscosity difference between the core and the annular layer, and a radially varying base flow. We have conducted a numerical study to explore the hydrodynamic stability of perfect core-annular flow in a narrow vertical tube under laminar conditions, considering three different types of flow: core-annular flow in (a) the absence of gravity and with a zero axial pressure gradient, (b) the presence of gravity and a zero axial pressure gradient, and (c)

---

* Corresponding author.
E-mail address: w.p.breugem@tudelft.nl (W.-P. Breugem).

https://doi.org/10.1016/j.ijmultiphaseflow.2026.105712
Received 20 June 2025; Received in revised form 1 March 2026; Accepted 30 March 2026

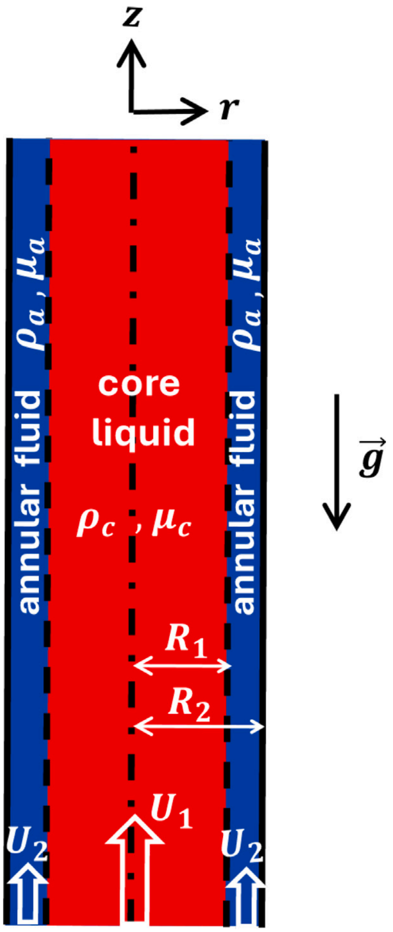

Fig. 1. Sketch of core-annular flow in a narrow vertical tube.

the presence of gravity and a non-zero axial pressure gradient, which approximately cancel each other. Many of the physical parameters used in our study to describe the flow, have been taken from Ooms and Pourquie (2024).

A sketch of the flow geometry is shown in Fig. 1. The core liquid and annular fluid are assumed to behave as Newtonian fluids. The flow is then characterized by 10 physical parameters: the radius of the liquid jet in the core (R_1), the radius of the tube (R_2), the dynamic viscosities of the fluid in the core (μ_c) and in the annulus (μ_a), the mass densities of the fluid in the core (ρ_c) and in the annulus (ρ_a), the surface tension coefficient (σ), the magnitude of the gravitational acceleration (g), and the bulk velocity in the core (U_1) and in the annular region (U_2).

From dimensional analysis, it follows that the flow is fully characterized by 7 dimensionless numbers. For the purpose of the present study, they are given as follows: (1) the Ohnesorge number for the core fluid, $Oh = \mu_c/\sqrt{\rho_c R_1 \sigma}$, (2) the Weber number based on the annular layer thickness, $We_a = \rho_a |U_1 - U_2|^2 (R_2 - R_1)/\sigma$, (3) the Bond number, $Bo = |\rho_c - \rho_a| g R_1^2/\sigma$, (4) the core-to-pipe radius ratio, R_1/R_2, (5) the core-to-annulus dynamic viscosity ratio, μ_c/μ_a, (6) the core-to-annulus density ratio, ρ_c/ρ_a, and (7) the core-to-annulus bulk velocity ratio, U_1/U_2. The choice of these dimensionless numbers is based on the fact that they are relevant for the interpretation of the simulation results later in this article.

In the present study, we consider narrow vertical tubes for which $Bo \ll 1$ in almost all cases, implying that surface tension effects dominate over the influence of gravity on the flow dynamics. This is not so much an assumption, but a consequence of the small tube radius chosen in our study to investigate a flow regime where capillary instabilities may be expected. Also, $\mu_c/\mu_a \gg 1$ in our study, which is typical for, e.g., oil/water two-phase flows in petrochemical applications. This indicates that viscous forces in the core fluid are much stronger than in the annular fluid. Related to this, $Oh = O(1)$ in almost all cases, indicating that both capillary (surface tension) forces and viscous forces within the core fluid are important. Under these conditions, the goal of our study is to gain insight in the hydrodynamic stability of perfect core-annular flow in narrow vertical tubes, in particular in the competition between capillary and shear-driven instability mechanisms. We have tested the temporal stability of the flow under a small-amplitude, axisymmetric sinusoidal perturbation of the interface using a finite-volume two-phase flow solver combined with a geometric Volume-of-Fluid (VOF) method for capturing the interface between the two immiscible fluids.

Since we consider an enclosed liquid jet in a *narrow* tube, we briefly discuss the hydrodynamic stability of *thin* liquid jets in free space. Eggers and Villermaux (2008) provide an excellent review of this topic, embracing many different types of liquid jets. Relevant to the present study is the so-called dispersion relation for a thin liquid jet in free space when subjected to a very small, axisymmetric wavy perturbation of the interface. In the long-wave limit of a linear stability analysis, the exponential growth or damping rate, ω_i, of a sinusoidal perturbation is given by Eggers and Villermaux (2008):

$$\omega_i = -\frac{3}{2}\frac{1}{\tau_V I_a}(kR_1)^2 + \frac{1}{\tau_I I_a}\sqrt{\left(\frac{3}{2}\,Oh\,k^2R_1^2\right)^2 + \frac{1}{2}I_a\left(k^2R_1^2 - k^4R_1^4\right)}$$
$$\text{for } \left(1 - \frac{9}{2}\frac{Oh^2}{I_a}\right)(kR_1)^2 \leq 1\,, \tag{1a}$$

$$\omega_i = -\frac{3}{2}\frac{1}{\tau_V I_a}(kR_1)^2$$
$$\text{for } \left(1 - \frac{9}{2}\frac{Oh^2}{I_a}\right)(kR_1)^2 \geq 1\,, \tag{1b}$$

where $k = 2\pi/\lambda$ is the wave number with λ the wave length, $\tau_I = \sqrt{\rho_c R_1^3/\sigma}$ is the capillary-inertial time scale and $\tau_V = \tau_I/Oh = R_1^2/\nu_c$ is the viscous damping time scale in the stable regime (i.e., the regime where the flow is not prone to a capillary instability). The factor I_a accounts for inertial effects of the perturbation flow in the annular region on the stability of the jet. Since $\mu_a/\mu_c \ll 1$ in the present study, viscous effects of the *perturbation* flow in the annular region are negligible and therefore are not taken into account. We remark that for the case of Eq. (1a) the sinusoidal perturbation will travel at a phase speed equal to the background jet velocity, while for the case of Eq. (1b) it will travel at a different phase speed.

When $k(R_2 - R_1) \gg 1$, the influence of the tube wall on the perturbation flow in the annular region near the jet interface can be neglected. In this case, I_a can be approximated by (see section 3.4.1. in Eggers and Villermaux, 2008):

$$I_a \approx 1 + \frac{1}{2}\frac{\rho_a}{\rho_c}(kR_1)^2 \ln\left(1 + \frac{1}{k^2R_1^2}\right) \quad \text{for } k(R_2 - R_1) \gg 1\,, \tag{2}$$

where it was implicitly assumed that the possible presence of an axial velocity difference of the background flow over the interface can be neglected. This correction factor becomes relevant when $\rho_a/\rho_c = O(1)$ and $Oh/\sqrt{I_a} \ll 1$, where $Oh/\sqrt{I_a}$ can be interpreted as an effective Ohnesorge number that accounts for the inertia of both the jet and the annular fluid.

For $Oh = 0$ and $\rho_a/\rho_c \ll 1$, Eq. (1a) reduces to a form first derived by Rayleigh (1879). This inviscid limit corresponds to the case of a capillary-inertial instability, where surface tension causes the instability and inertia of the liquid slows it down but cannot avoid it. For large values of Oh, Eq. (1a) can be further approximated by:

$$\omega_i \approx \frac{1}{6\,\tau_{CV}}\left(1 - k^2R_1^2\right) \quad \text{for} \quad \frac{Oh}{\sqrt{I_a}} \gg \sqrt{\frac{2}{9}\left|\frac{1}{k^2R_1^2} - 1\right|}\,, \tag{3}$$

where $\tau_{CV} = \tau_V\,Oh^2 = \mu_c R_1/\sigma$ is the capillary-viscous time scale.

Note that a negative growth rate implies exponential damping of the associated perturbation and hence a stable flow. Furthermore, irrespective of the value of $Oh/\sqrt{I_a}$, $\omega_i > 0$ for $kR_1 < 1$. This implies that the jet is unstable for any perturbation with a wave length larger than the circumference of the undisturbed jet, a well-known result from experiments by Plateau (1873) and theoretical work of Rayleigh (1879). Conversely, $\omega_i < 0$ for $kR_1 > 1$ and the flow is thus stable for wave lengths smaller than the jet circumference. Finally, provided that the variation of I_a with kR_1 is relatively weak and can be neglected, it follows from Eq. (1a) that the wave length of the fastest growing perturbation is approximately equal to $\lambda_{\text{opt}} \approx 2\pi R_1 \left(2 + 3\sqrt{2}\, Oh/\sqrt{I_a}\right)^{\frac{1}{2}}$; for small values of ρ_a/ρ_c this is a valid approximation anyway. These results from stability theory for liquid jets proved to be highly relevant for the present study, and are used to interpret our numerical results.

The remainder of this manuscript is organized as follows. In Section 2, the numerical method is explained and details are given of the computational setup of the simulations. In Section 3, the results are presented for three different flow types: core-annular flow in the absence of gravity and with a zero axial pressure gradient (Section 3.1), core-annular flow in the presence of gravity and a zero axial pressure gradient (Section 3.2), and finally core-annular flow in the presence of both gravity and a non-zero axial pressure gradient (Section 3.3). In Section 4, the main conclusions are summarized, followed by a discussion and perspectives for future work.

2. Numerical method and computational setup

The numerical simulations were performed with the two-phase incompressible flow solver interFoam (Deshpande et al., 2012) in the open-source software OpenFOAM (Weller et al., 1998) (version 8) for Computational Fluid Dynamics (CFD). An explicit, geometric VOF method was employed, based on a multicut Piecewise Linear Interface Construction (PLIC) (J.S. Piña et al., 2022), to capture the interface between the two immiscible fluids in space and time. The advection equation for the VOF function was solved in conjunction with the Navier–Stokes and mass conservation equations for an axisymmetric (2D) flow using a finite-volume discretization on a fixed, collocated grid. An orthogonal and equispaced computational grid was used for the present simulations. Surface tension was incorporated in the momentum equations through the Continuous Surface Force (CSF) model (Brackbill et al., 1992). Details of the numerical approach and an evaluation of the interFoam solver performance are provided by Deshpande et al. (2012).

The following discretization schemes were applied in our simulations: backward Euler in time, a second-order limited scheme based on the TVD framework (Sweby, 1984) for the advection terms of the velocity components, and the van Leer scheme for the advection of the VOF field. Pressure−velocity coupling was performed using the PIMPLE scheme. A preconditioned conjugate gradient method and a preconditioned biconjugate gradient method were used as linear solvers for the pressure and the velocity components, respectively.

In the simulations, a no-slip condition was applied at the tube wall and a free-slip (symmetry) condition at the tube centerline. At the tube inflow and outflow planes, a periodic boundary condition was applied, implying that the length (l) of the computational domain was equal to an integer number of perturbation wavelengths at the core-annular interface. The initial velocity distribution was chosen to be equal to the analytical solution of the Navier–Stokes equations for laminar core-annular flow with a smooth, cylindrical interface, see Appendix A.

To study the hydrodynamic stability of the flow, the core-annular interface was disturbed by a cosine wave with a small amplitude according to $R_i(z) = R_1 - A\cos(2\pi z/\lambda)$, where R_1 is the nominal jet radius, A is the initial perturbation amplitude, z is the axial coordinate and λ is the perturbation wave length. Based on the prescribed perturbation of the interface, the liquid volume fraction was computed for every grid cell, which served as initial condition for the VOF field.

The computational time step was determined from the following constraint for numerical stability:

$$\Delta t = \min\left(\Delta t^{\text{co}}_{\max},\ \alpha\, \Delta t^{\text{cap}}_{\max}\right), \tag{4}$$

where $\Delta t^{\text{co}}_{\max} = Co \cdot V_{\text{cell}} / \left(\frac{1}{2}\sum_i |\phi_i|\right)$ with Co the Courant number set equal to $Co = 0.02$ in our simulations, V_{cell} is the grid cell volume, $\sum_i |\phi_i|$ is the sum over the absolute volume fluxes across all the grid cell faces, and $\Delta t^{\text{cap}}_{\max}$ is the maximum allowed time step set by surface tension with the prefactor α being a safety factor. In the present study, we used $\alpha \approx 0.5$. In Appendix B, a derivation is given of the analytical expression for $\Delta t^{\text{cap}}_{\max}$ used in the present study. In Appendix C, the time step criterion given by Eq. (4) is evaluated for one of the cases discussed in the next section. Based on this, we conclude that our time step criterion suffices to maintain a numerically stable integration.

In Appendix D, results are presented from a grid convergence study for the same case for which the time step criterion was evaluated. Based on this, we selected a default grid resolution for our simulations corresponding to 192 cells over the tube radius and 192 grid cells along each wave of the imposed perturbation in the axial direction.

3. Results

3.1. Gravity absent and zero pressure gradient

Let us conceive, first, a circular jet of a viscous fluid enclosed by a much less viscous and much less dense fluid in a narrow tube. In the absence of gravity and with a zero background pressure gradient, both fluids are initially at rest. We investigate under what circumstances the jet is stable or unstable under a small, axisymmetric, wavy perturbation of the jet interface owing to the operation of a capillary force.

Seven cases have been simulated to study the hydrodynamic stability of the flow, where the first case served as the reference case for the other cases. Table 1 lists the spatial grid resolution used, the flow parameters that were varied (R_1, l and ν_c), the parameters of the imposed perturbation (A and λ), the dimensionless wave number ($2\pi R_1/\lambda$), and the Ohnesorge number (Oh) of the simulated cases. Since the inertial correction factor (I_a) given by Eq. (2) is very close to one, indicating negligible inertial effects from the annular fluid on the jet dynamics, it is not included in the table. In all cases, the radius of the tube is $R_2 = 0.00475547$ m, the density of the core fluid is $\rho_c = 905$ kg/m^3, the density of the annular fluid is $\rho_a = 1$ kg/m^3, the kinematic viscosity of the annular fluid is $\nu_a = 10^{-6}$ m^2/s, and the surface tension coefficient is $\sigma = 0.01$ kg/s^2. Since the dynamic viscosity of the annular fluid ($\mu_a = \rho_a\nu_a$) is always much smaller than the dynamic viscosity of the core ($\mu_c = \rho_c\nu_c$), viscous effects of the annular fluid on the jet dynamics are negligible too.

In five cases, the wave length of the perturbation is longer than the circumference of the circular liquid jet (unstable perturbation). In two cases, the wave length is shorter (stable perturbation). In cases expected to be unstable, a small perturbation amplitude of $A = 2 \cdot 10^{-5}$ m was set, while in cases expected to be stable, the perturbation amplitude was deliberately set much larger to test whether these cases would indeed remain stable. In cases 1–3, the jet radius was varied. In cases 1, 4, and 5, we varied the domain length. In cases 1 and 6, the wave length of the perturbation was varied. Finally, in cases 1 and 7, the viscosity of the jet was varied.

Case 1: The dimensionless wave number, $2\pi R_1/\lambda = 0.542$, is smaller than one in this case, and hence the flow is expected to be unstable to the given perturbation. The Ohnesorge number is equal to $Oh = 6.31$. This high value is caused by the high viscosity of the core fluid. This is an indication that inertial effects of the core fluid are negligible and that the instability is driven by surface tension and counteracted by viscous effects in the core. From Eq. (1a), the most unstable wave length (i.e., with the largest growth rate) would correspond to $\lambda_{\text{opt}}/l = 2.905$,

Table 1

Cases studied for a circular jet of a viscous fluid enclosed inside a narrow tube by another fluid, both at rest in the absence of gravity and with a zero background pressure gradient. The second column shows the spatial grid resolution in terms of the number of grid cells in the radial (N_r) and the axial (N_z) direction. Columns 3–7 show, respectively, the jet radius of the base flow (R_1), the length of the periodic tube (l), the kinematic viscosity of the core fluid (ν_c), the perturbation wave length (λ) and the initial perturbation amplitude (A). The last two columns list, respectively, the normalized wave number of the prescribed perturbation ($2\pi R_1/\lambda$) and the Ohnsesorge number (Oh).

Case	$N_r \times N_z$	R_1 (m)	l (m)	ν_c (10^{-4} m^2/s)	λ (m)	A (10^{-5} m)	$2\pi R_1/\lambda$	Oh
1	192 × 192	0.001	0.0116	6.63	0.0116	2	0.542	6.31
2	192 × 192	0.0015	0.0116	6.63	0.0116	2	0.812	5.15
3	192 × 192	0.003	0.0116	6.63	0.0116	100	1.625	3.64
4	192 × 768	0.001	0.0464	6.63	0.0116	2	0.542	6.31
5	192 × 1536	0.001	0.0928	6.63	0.0116	2	0.542	6.31
6	192 × 192	0.001	0.0116	6.63	0.00387	50	1.625	6.31
7	192 × 192	0.001	0.0116	0.0663	0.0116	2	0.542	0.0631

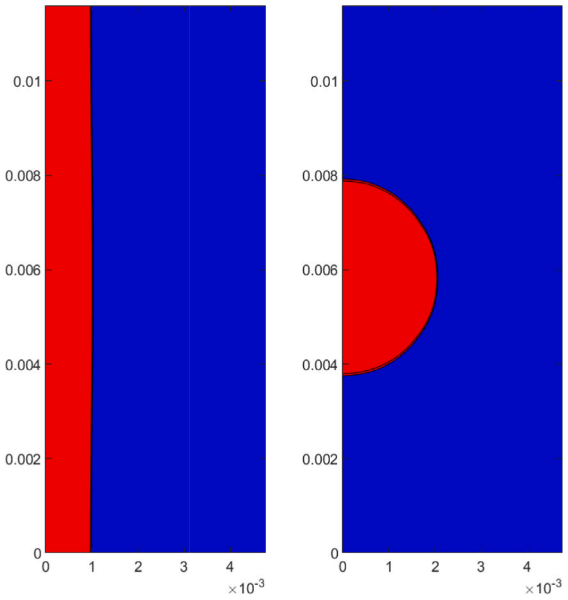

Fig. 2. Development of the flow topology for case 1 of Table 1. Colors denote the spatial distribution of the core (red) and the annular fluid (blue). Black contours represent two isolines of the VOF function and mark the interface between the two fluids. Spatial coordinates are given in units of meter. Left panel: $t = 0$ s. Right panel: $t = 8.18$ s. (For interpretation of the references to color in this figure legend, the reader is referred to the web version of this article.)

which does not fit in the periodic simulation domain. This implies that the current perturbation with $\lambda = l$ corresponds to the unstable wave length with the largest *possible* growth rate and hence 1 drop is expected after jet breakup.

The results for case 1 are presented in Fig. 2 and Figs. 19 and 20 in Appendix D, showing the change in the flow topology, the evolution of the normalized perturbation amplitude and the location of the minimum jet radius as a function of time, respectively. The starting time of the initial perturbation is defined as $t = 0$ s. Thereafter, the perturbation amplitude increases exponentially with time, ultimately resulting in breakup of the jet at $t \approx 2$ s and the subsequent formation of 1 drop. Because of the large value of Oh, the exponential growth rate of the initial perturbation is governed by Eq. (3). This is confirmed by Fig. 19. The growth of the perturbation during the early stage is in excellent agreement with the exponential growth rate of $\omega_i = 1.963$ s^{-1} predicted by Eq. (3).

Case 2: The simulation of case 1 was repeated, but this time with $R_1 = 0.0015$ m. The Ohnesorge number, $Oh = 5.15$, is a bit smaller than before but still large. Furthermore, the dimensionless wave number, $2\pi R_1/\lambda = 0.812$, remains smaller than 1, and hence an unstable case is expected as before. Again, the given perturbation corresponds to the most unstable *possible* wave length. The result is once more a single drop, see Fig. 3. The exponential growth of the perturbation during the early stage is in excellent agreement with the exponential growth rate of $\omega_i = 0.629$ s^{-1} predicted from Eq. (3). After jet breakup, the perturbation amplitude reaches a constant value, which is in excellent agreement with the expected drop radius of $R_d = (3R_1^2 l/4)^{1/3}$ based on mass conservation and the assumption of a perfectly spherical drop.

Case 3: The simulation of case 1 was repeated again, but this time with $R_1 = 0.003$ m. The Ohnesorge number is $Oh = 3.64$, which is still large. The dimensionless wave number, $2\pi R_1/\lambda = 1.625$, is well beyond 1, and hence a stable flow can be expected under this perturbation. To test this hypothesis, the simulation was initiated with a large perturbation amplitude of $A = 10^{-3}$ m, which is 50 times higher than in the previous unstable cases. The result is shown in Fig. 4. Indeed, the perturbation quickly damps and the flow topology returns to a perfect core-annular flow. After a small initial transient of about 1 s, in which the flow has to adapt to the large perturbation of the core-annular interface, the perturbation amplitude decays approximately in an exponential manner. The decay rate is in good agreement with Eq. (3), but only when R_1 is replaced by R_1^*, where $R_1^* = R_1\sqrt{1 + A^2/(2R_1^2)} = 3.082 \cdot 10^{-3}$ m is the apparent jet radius that accounts for the finite perturbation amplitude such that $\pi(R_1^*)^2\lambda = \int_0^\lambda \pi R_i^2\, dx$. Furthermore, the good agreement with Eq. (3) indicates that the exponential decay originates from both capillary and viscous damping.

Case 4: Again, the simulation of case 1 was repeated, but this time for a periodic tube that was 4 times longer. All other parameters, including the wave length, were kept the same, so exactly 4 waves fitted within the domain in this case. The perturbation grows at the same exponential growth rate and breaks up in a similar manner as before, but now resulting in 4 drops, see Fig. 5. The most optimal wave length with the highest growth rate corresponds to $\lambda_{\text{opt}} = 0.726\, l$ based on Eq. (1a). This wave does not fit within the periodic domain, but waves with $\lambda = l/3$, $l/2$ and l do fit in the periodic domain and all have a higher growth rate than the given perturbation with $\lambda = l/4$. Fig. 5 indicates that the given perturbation is nevertheless sufficiently strong to dominate the breakup process. Hence, 4 drops were generated instead of 1, 2 or 3 drops corresponding to, respectively, $\lambda = l$, $l/2$ and $l/3$.

Case 5: The simulation of case 1 was also repeated for a periodic tube that was 8 times longer. The perturbation wave length was again kept fixed, so 8 waves fitted within the domain now. The exponential growth occurred at the same growth rate as in case 1 and resulted in a similar breakup process. As expected, 8 drops were formed in this case (not shown).

Case 6: Again, the simulation of case 1 was repeated, but this time with $\lambda = l/3$, so with three shorter waves over the same domain length.

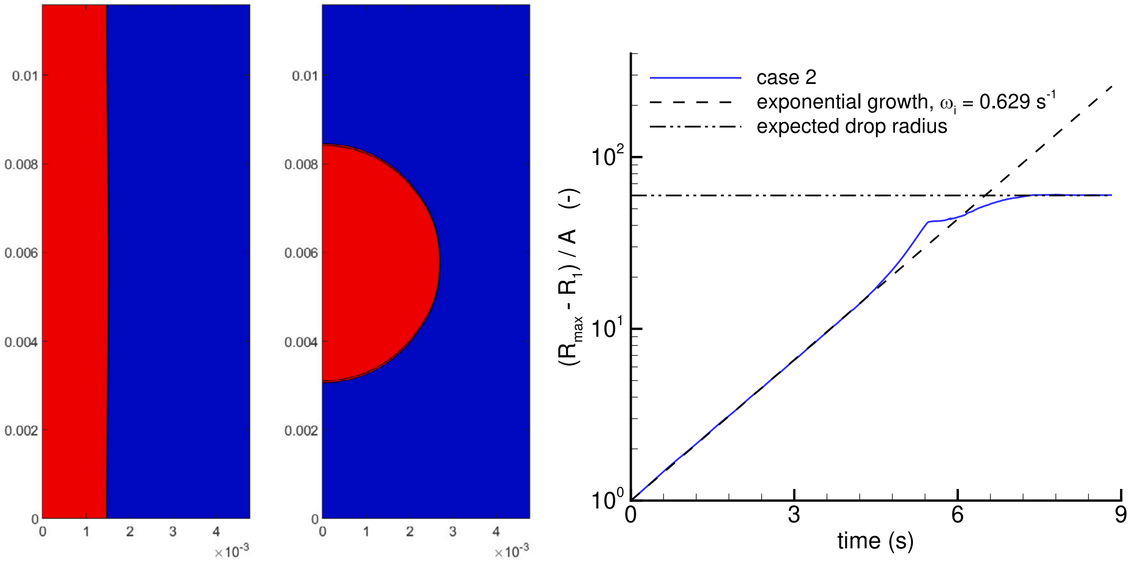

Fig. 3. Development of the flow topology for case 2 of Table 1. Left panel: $t = 0$ s. Middle panel: $t = 8.83$ s. Right panel: evolution of the normalized perturbation amplitude, $(R_{\max}(t) - R_1)/A$, as a function of time, where $R_{\max}(t)$ is the maximum jet radius, R_1 is the nominal jet radius and A is the initial perturbation amplitude. The dashed line corresponds to an exponential growth at a growth rate computed from Eq. (3). The dash-dotted line corresponds to the expected final drop radius.

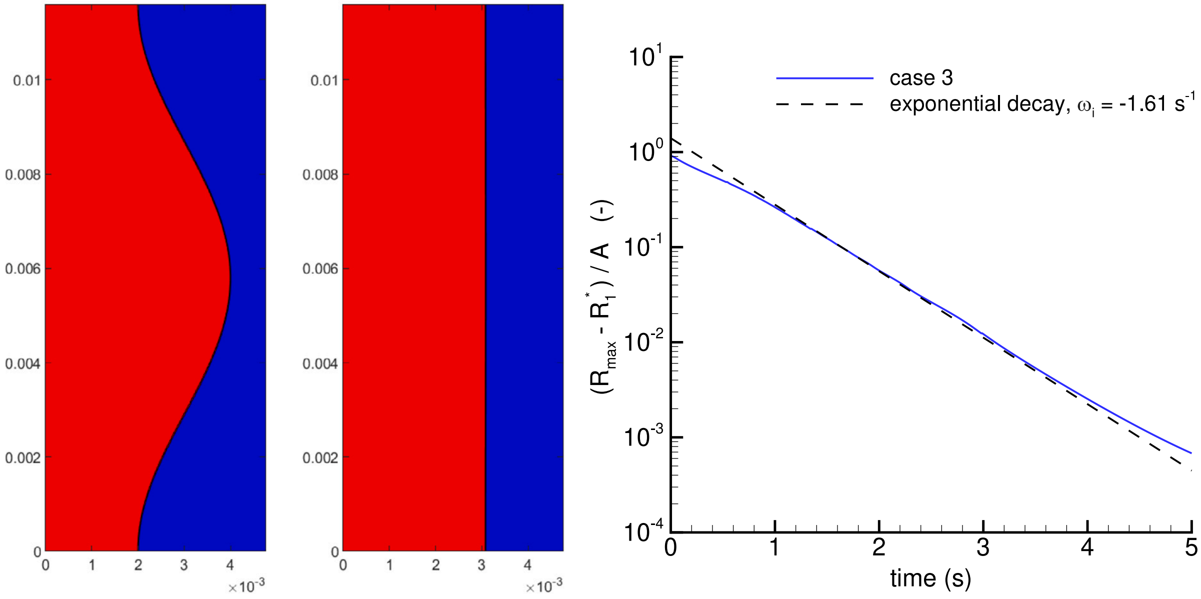

Fig. 4. Development of the flow topology for case 3 of Table 1. Left panel: $t = 0$ s. Middle panel: $t = 4$ s. Right panel: evolution of the normalized perturbation amplitude, $(R_{\max}(t) - R_1^*)/A$, as a function of time, where R_1^* is the *apparent* nominal jet radius. The dashed line corresponds to an exponential decay at a decay rate computed from Eq. (3).

The dimensionless wave number is now $2\pi R_1/\lambda = 1.625$, which is significantly larger than 1 and hence a stable flow can be expected under this perturbation. To test this, the initial perturbation amplitude was deliberately set 25 times larger than in case 1, see Table 1. The result is shown in Figs. 6 and 7.

Indeed, the initial perturbation is strongly damped and vanishes completely. Ignoring the initial transient during the first second, Fig. 7 (left panel) shows an exponential decay of the initial perturbation. The decay rate is in good agreement with the prediction from Eq. (3), provided that the *apparent* jet radius is used, $R_1^* = R_1\sqrt{1 + A^2/(2R_1^2)} = 1.061 \cdot 10^{-3}$ m. However, when time progresses, the smooth interface becomes unstable and ultimately 1 drop is formed, centered around the periodic domain boundaries, see the right panel in Fig. 6. While the flow is stable under the initial perturbation, the jet is still prone to a capillary-viscous instability for larger wave lengths that fit within the computational domain and for which $kR_1 < 1$. The largest *possible*

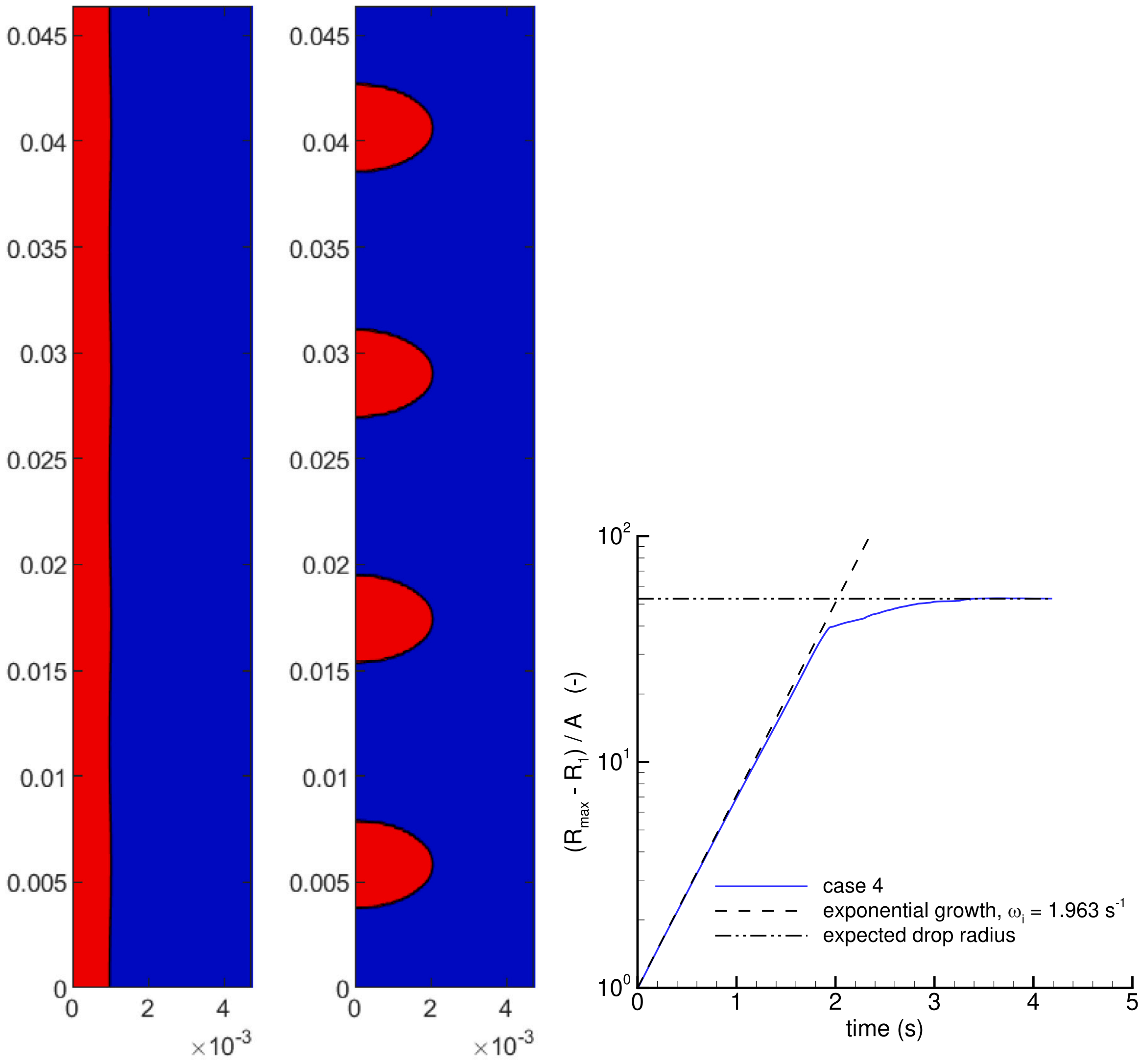

Fig. 5. Development of the flow topology for case 4 of Table 1. Left panel: $t = 0$ s. Middle panel: $t = 3.81$ s. Right panel: evolution of the normalized perturbation amplitude as a function of time. The dashed line corresponds to an exponential growth at a growth rate computed from Eq. (3). The dash-dotted line corresponds the expected final radius of the drops.

wave length with the highest growth rate corresponds to $\lambda = l$, similar to case 1, which explains why the jet ultimately breaks up into 1 drop. Numerical noise related to, e.g., slight variations in jet curvature might have been the trigger for the final instability. The exponential growth rate of the perturbation at later times is again in excellent agreement with Eq. (3) when R_1 is replaced by R_1^*, see Fig. 7 (left panel).

Fig. 7 (right panel) shows the position of the minimum and the maximum jet radius during flow development. Initially, 3 minima and 3 maxima are present, consistent with the 3 perturbation waves that were prescribed. After roughly 1 s, only 1 minimum and 1 maximum are left over, which slowly move in the downward direction for unclear reason, except for a small kink between $t \approx 2$ and $t \approx 3$ s. Interestingly, once the maximum reaches the periodic domain boundaries at $t \approx 7$ s, it remains pinned, and this seems to coincide with the moment of droplet pinch-off.

Case 7: To test the influence of the core viscosity, the simulation of case 1 was repeated with a 100 times smaller core viscosity. The Ohnesorge number is now $Oh = 6.31 \cdot 10^{-2}$, which is small and hence the breakup of the jet is expected to be dominated by a capillary-inertial instability. Based on Eq. (1a), the wave length with the highest growth rate corresponds to $\lambda_{\text{opt}} = 0.816\,l$. Since $kR_1 > 1$ for $\lambda = l/2$ (thus a stable flow), this implies that the imposed perturbation with $\lambda = l$ is the only *possible* wave with a positive growth rate that fits within the domain. For the corresponding dimensionless wave number of $kR_1 = 0.542$, Eq. (1a) predicts an exponential growth rate of $\omega_i = 31.05$ s^{-1}. This can be compared with the prediction based on the original theory of Rayleigh (1879) for an inviscid liquid jet by evaluating Eq. (1a) for $\tau_V \to \infty$ and $Oh = 0$: $\omega_i = 33.84$ s^{-1}. Ignoring viscous effects thus results in an overestimation of the growth rate by approximately 9%. So, although viscosity plays a minor role, it has still a non-negligible effect.

The results for case 7 are shown in Figs. 8 and 9. As expected, the imposed perturbation exhibits exponential growth during the initial phase. The exponential growth rate is in excellent agreement with the

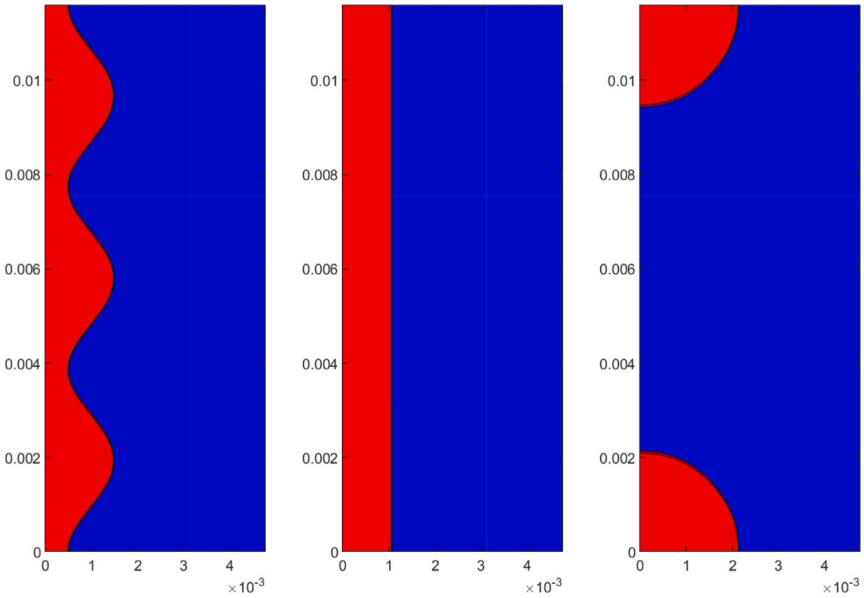

Fig. 6. Development of the flow topology for case 6 of Table 1. Left panel: t = 0 s. Middle panel: t = 3.00 s. Right panel: t = 9.00 s.

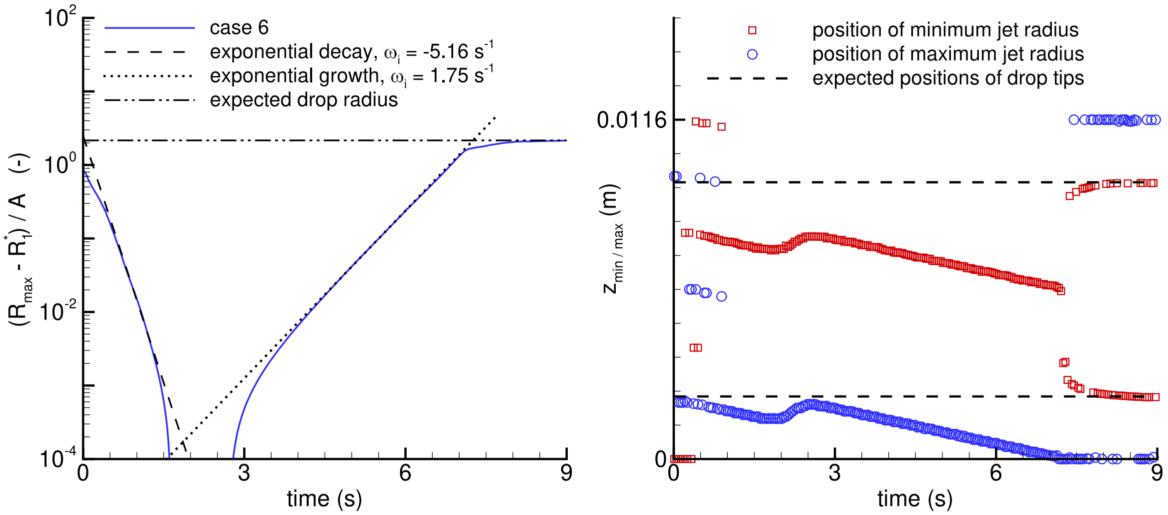

Fig. 7. Left panel: evolution of the normalized perturbation amplitude as a function of time for case 6 of Table 1. The dashed and the dotted line correspond to, respectively, an exponential decay and an exponential growth of the perturbation amplitude according to Eq. (3). The dash-dotted line corresponds to the expected final radius of the drop ultimately formed. Right panel: position of the minimum and the maximum jet radius as a function of time during the development of the flow. The simulation data was sampled every 0.04 s. The dashed lines indicate the expected edges of the final drop in the axial direction when the drop is centered around the periodic domain boundaries at $z = 0$ and $z = l$.

prediction from Eq. (1a). At $t \approx 0.15$ s, the jet breaks up, but this does not immediately result in 1 drop as expected, but in the formation of 1 smaller and 1 larger oscillating drop. The reason for this is unclear, but it might be a non-linear effect, since the perturbation amplitude is no longer small just before jet breakup. Shortly after this, the smaller drop coalesces with the larger drop at the bottom tip of the larger drop. This results in a single drop that moves slightly upward at a velocity of ≈ 0.042 m/s. This is of the same order as the capillary-inertial velocity scale, $\sqrt{\sigma/(\rho_c R_d)} = 0.073$ m/s, obtained from balancing the kinetic energy of the new drop with the release of free surface energy due to merging of the 2 drops and the subsequent shape retraction.

As visible from Fig. 9, the newly formed drop exhibits strong shape oscillations with a time period of ≈ 0.08 s. The amplitude of the oscillations decreases over time and is almost zero at $t \approx 1$ s. The oscillation period can be compared with the prediction based on the Rayleigh–Lamb theory (Rayleigh, 1879; Lamb, 1881) for the fundamental time period of a damped oscillating drop (prolate/oblate) in free space:

$$\tau_{\text{osc}} = 2\pi \sqrt{\frac{\rho_c R_d^3/(8\sigma)}{1-(25/8)Oh_d^2}}\,, \tag{5}$$

where $Oh_d = \mu_c/\sqrt{\rho_c R_d\,\sigma} = 4.40 \cdot 10^{-2}$ is the Ohnesorge number for the drop based on the volume-equivalent sphere diameter. This yields $\tau_{\text{osc}} = 0.0625$ s for the present case. Since Oh_d is small, the drop viscosity appears to have a negligible effect on the oscillation period. The theoretical prediction underestimates the actual oscillation time by more than 20%, possibly due to the large oscillation amplitude, which invalidates the linearization underlying the Rayleigh–Lamb theory. Lamb's theory (Lamb, 1881) predicts that the oscillation amplitude is exponentially damped by viscosity with a decay time of $\tau_{\text{decay}} = \rho_c R_d^2/(5\mu_c) = 0.128$ s. Interestingly, between $t \approx 0.5$ and 1 s, this appears

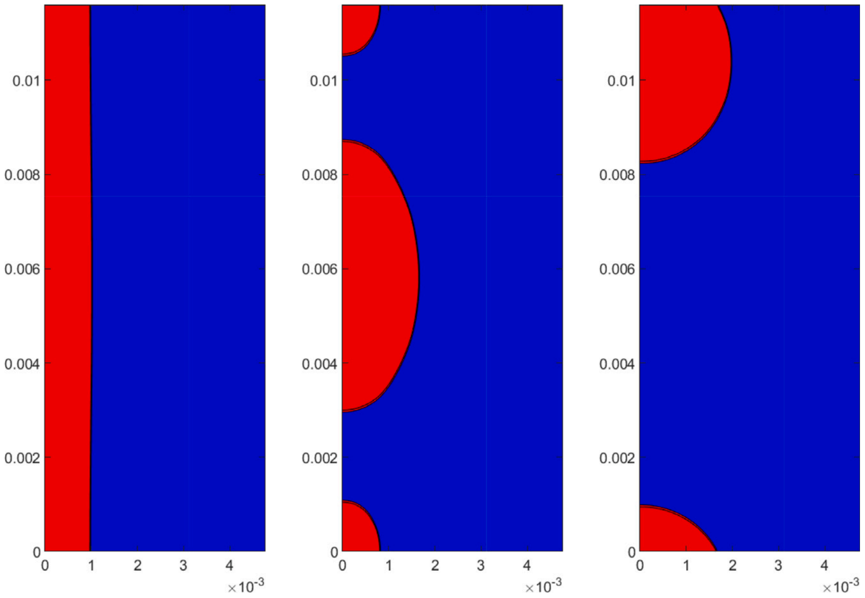

Fig. 8. Development of the flow topology for case 7 of Table 1. Left panel: t = 0 s. Middle panel: t = 0.18 s. Right panel: t = 1.63 s.

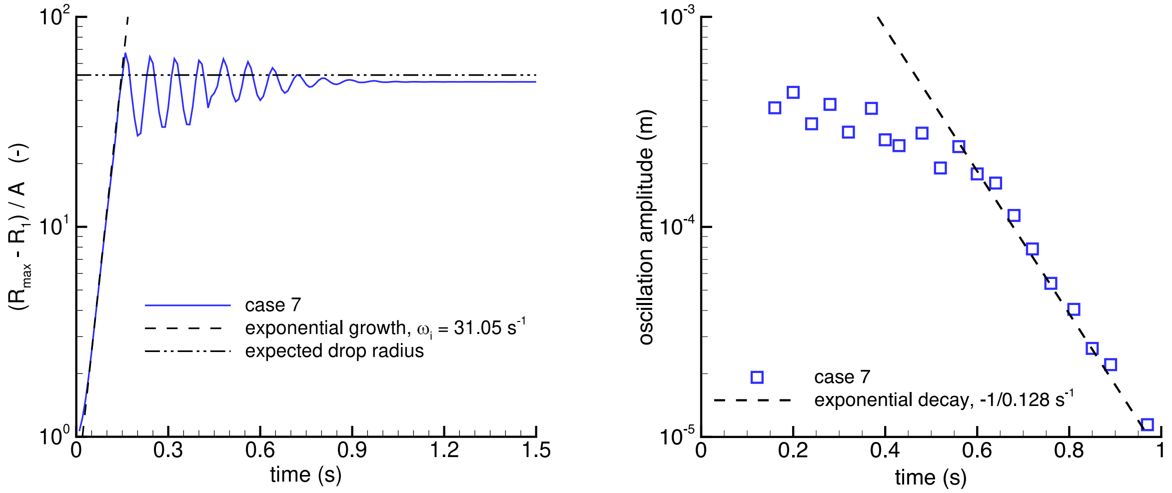

Fig. 9. Left panel: evolution of the normalized perturbation amplitude as a function of time for case 7 of Table 1. The dashed line corresponds to an exponential growth of the perturbation amplitude according to Eq. (1a). The dash-dotted line corresponds to the expected radius of the drop ultimately formed, based on mass conservation and assuming a perfectly spherical shape. Right panel: decay of the amplitude of the oscillations in $R_{\max}$ with respect to the equilibrium radius at large times. The dashed line corresponds to an exponential decay at a rate of $1/0.128$ s^{-1}.

to capture the decay in the perturbation amplitude remarkably well, see Fig. 9 (right panel).

Finally, Fig. 9 (left panel) shows that the equilibrium perturbation amplitude after jet breakup is slightly less than the expected drop radius based on mass conservation and assuming a perfectly spherical drop. In fact, the shape of the drop closely resembles a prolate spheroid, being slightly more stretched in the axial direction and slightly flattened in the radial direction. Compared to the volume-equivalent sphere radius of $R_d \approx 2.06 \cdot 10^{-3}$ m, the semi-major and semi-minor radii of the prolate are approximately $2.18 \cdot 10^{-3}$ m (+5.7%) and $1.98 \cdot 10^{-3}$ m (−3.7%), respectively. The slightly non-spherical shape is likely a numerical artifact related to discretization errors in the calculation of the interface curvature and hence the surface tension; see Appendix D, where a similar problem was observed in the simulation of case 1 with the 128 × 128 grid.

3.2. *Gravity present and zero pressure gradient*

The previous study was repeated, but now with gravity present. The background pressure gradient is still zero. Since the base flow is non-zero in this case, the flow may be prone to both capillary and shear-driven instabilities, depending on the flow parameters. Three cases have been simulated in which we varied the core radius (R_1) and the surface tension coefficient (σ), see Table 2. They are labeled as cases 8–10 with case 8 serving as the reference case. In all cases, the length of the periodic tube is $l = 0.0464$ m, the tube radius is $R_2 = 0.00475547$ m, the kinematic viscosity of the core fluid is $\nu_c = 6.63 \cdot 10^{-4}$ m^2/s, the kinematic viscosity of the annular fluid is $\nu_a = 1.1 \cdot 10^{-5}$ m^2/s, the density of the core liquid is $\rho_c = 905$ kg/m^3, the density of the annular fluid is $\rho_a = 995$ kg/m^3, and the magnitude of the gravitational acceleration is $g = 9.81$ m/s^2.

The length of the periodic tube was chosen the same as in case 4 of the previous study. Ideally, the length should be as large as

Table 2
Cases studied for a circular jet of a viscous fluid enclosed inside a narrow tube by another fluid, in the presence of gravity and with a zero background pressure gradient. The second and the third column show the two parameters that have been varied in the simulations: the nominal radius of the jet in the core (R_1) and the surface tension coefficient (σ). The last 5 columns list dimensionless numbers derived from the flow parameters.

Case	R_1 (m)	σ (kg/s^2)	$2\pi R_1/\lambda$	$Oh/\sqrt{I_a}$	I_a	Bo	We_a
8	0.0037192	0.2	2.015	0.53	1.90	$6.11 \cdot 10^{-2}$	4.46
9	0.0037192	0.01	2.015	2.37	1.90	1.22	89.3
10	0.001	0.2	0.542	1.30	1.17	$4.41 \cdot 10^{-3}$	57.3

possible, to avoid the influence of the finite tube length and the periodic boundary conditions on hydrodynamic instabilities that may develop. The chosen length in the current study was a compromise to limit the computational costs of the simulations.

The dynamic viscosity of the annular fluid ($\mu_a = \rho_a \nu_a$) is more than 10^4 times higher than before. This was deliberately chosen much higher to limit the fall velocity of the fluids under gravity, see Appendix A. Note that the dynamic viscosity of the annular fluid is still more than 50 times smaller than the dynamic viscosity of the core ($\mu_c = \rho_c \nu_c$), so the *direct* influence of the viscosity of the annular fluid on the *perturbation* flow can still be neglected.

Different from the previous study, the densities of the core and the annular fluid are now fairly close to each other. This is also reflected in the inertial correction factor (I_a), which is significantly larger than 1, see Table 2. This implies that inertial effects from the annular flow cannot be neglected anymore relative to inertial effects from the core. For this reason, Table 2 shows the value of $Oh/\sqrt{I_a}$ instead of Oh, as the latter does not account for the inertia of the annular fluid. The value of $Oh/\sqrt{I_a}$ is smallest for case 8, suggesting that inertial effects from both the core and the annular fluid on the perturbation flow are non-negligible in this case.

In Table 2, also the Bond number for the jet in the core is included. It quantifies the importance of the hydrostatic pressure difference over the jet interface of $O(|\rho_c - \rho_a| g R_1)$, assuming that the perturbation wave length $\lambda = O(R_1)$, compared to the Laplace pressure of $O(\sigma/R_1)$. In cases 8 and 10, $Bo \ll 1$, suggesting that gravity does not have a strong *direct* influence on the development of flow instabilities, although there is still an *indirect* effect through the influence of gravity on the base flow. However, $Bo = O(1)$ in case 9, and here gravity might affect the development of flow instabilities in a direct manner; this will be discussed later.

The velocity profiles of the smooth base flow are shown in Fig. 17 in Appendix A. The profiles for cases 8 and 9 are the same, since surface tension does not affect the base flow (except for a jump in the pressure over the core-annular interface). The stability of the core-annular flow was tested under a sinusoidal perturbation with 4 waves over the tube length, so $\lambda = l/4 = 0.0116$ m, and a small initial perturbation amplitude, $A = 2 \cdot 10^{-5}$ m. The simulations were performed at a fixed grid resolution of $N_r \times N_z = 192 \times 768$ in all 3 cases.

Case 8: The dimensionless wave number, $2\pi R_1/\lambda = 2.015$, is well beyond 1, so no capillary instability is expected under the given perturbation. The modified Ohnsesorge number, $Oh/\sqrt{I_a}$, is equal to 0.53. Under these conditions, Eq. (1a) can be used to estimate the capillary-viscous damping rate: $\omega_i = -55.8$ s^{-1}. We remark that the damping rate drops by approximately 10.5% when $I_a = 1$ would be assumed, i.e., when the inertia of the annular fluid would not be taken into account. Thus, the effect of the inertia of the annular fluid is small, but still significant. It should be noted here that $k(R_2 - R_1) = 0.56$, which suggests that the effect of the tube wall on the perturbation flow in the annular region cannot be ignored actually. The tube wall will likely have an influence on our estimate of the inertial correction factor, and hence on the decay rate, but it is difficult to assess this effect in a more quantitative manner.

The result for the normalized perturbation amplitude obtained from the simulation of case 8, is shown in Fig. 10. The simulated decay rate is in reasonably good agreement with the prediction. It should be taken into account here that the initial perturbation is small, and only a factor 1.24 times larger than the radial dimension of the grid cells. Since the maximum jet radius is based on the VOF = 0.5 isocontour obtained from linear interpolation, the error in the radius is expected to be $O(\Delta r)$. This likely explains the serrated profile for the perturbation amplitude during the early stage of development and the non-zero equilibrium value for $t \gtrsim 0.1$ s.

During the early stage, the sinusoidal perturbation waves travel downwards along the core-annular interface at a velocity of approximately -1.6 m/s. This is somewhat lower than the expected interface velocity of the analytical base flow of approximately -1.82 m/s. This reason for this is not fully clear, but it might be related to the diffuse representation of the interface in which the viscosity jump over the interface is smeared out over a few grid cells. It is left for future research to study this in more detail.

Although the flow is stable under the given perturbation, the flow is still prone to a capillary-viscous instability under a perturbation with a longer wave length equal to $\lambda = l$, since this corresponds to $2\pi R_1/\lambda = 0.504$ and is therefore less than 1. The corresponding exponential growth rate can be computed from Eq. (1a) and yields $\omega_i = 8.74$ s^{-1}. Furthermore, the flow might also be sensitive to a shear-driven instability.

We have run the simulation till $t \approx 1.3$ s, but the flow remained stable. Although it cannot be excluded that an instability may develop at larger times, we decided to abort the simulation to limit the computational costs.

Case 9: Since this case differs from the previous case only for the much lower surface tension coefficient, the dimensionless wave number is still the same and hence no capillary instability is expected under the given perturbation. However, the predicted capillary-viscous decay rate is much weaker in this case because of the much lower surface tension coefficient: $\omega_i \approx -2.3$ s^{-1} based on Eq. (1a) or Eq. (3). Furthermore, as for the previous case, the flow is prone to a capillary instability at a wave length of $\lambda = l$.

The development of the flow topology for case 9 is shown in Fig. 11. Interestingly, instead of capillary-viscous damping of the imposed perturbation, an instability has developed. At $t = 0.24$ s, 16 waves are present over the domain height, corresponding to an average wave length 4 times smaller than the wave length of the initial perturbation. Since the short wave length corresponds to a dimensionless wave number much larger than one ($2\pi R_1/\lambda = 8.1$), this must be a shear-driven instability. The waves are characterized by steep crests and smooth troughs. At $t = 0.98$ s, the instability has evolved further and resulted in an irregular and rough core-annular interface. Shorter and longer waves can be observed, with the wave length varying between ~ 0.002 and 0.006 m. The relative motion between the viscous liquid core and the annular fluid deflects the wave crests in the upward direction and creates thin liquid sheets. Small liquid fragments are continuously pinched off from these sheets, and are entrained into the flow in the annular region. It should be noted here that the assumption of axisymmetry of the flow used to justify the present axisymmetric (2D) simulations, is questionable from the moment onward the axisymmetric liquid fragments are pinched off from the jet. Such ring-shaped structures are presumably unstable and will likely disintegrate into smaller spherical droplets.

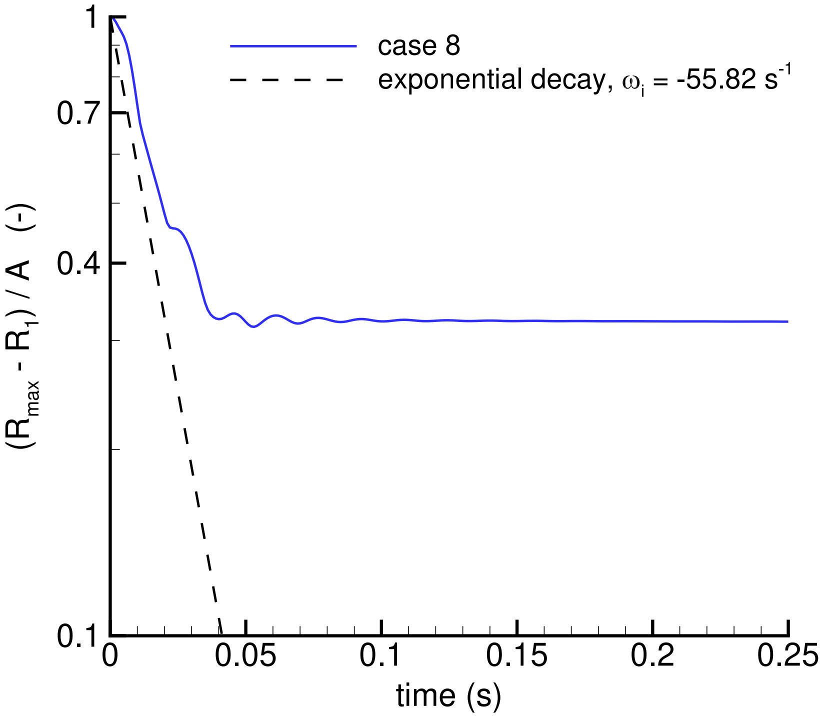

Fig. 10. Evolution of the normalized perturbation amplitude as a function of time for case 8 of Table 2. The dashed line corresponds to an exponential decay of the perturbation amplitude according to Eq. (1a).

The observed flow instabilities are reminiscent of the primary and secondary instabilities in the atomization of a liquid jet by a co-axial gas flow (Marmottant and Villermaux, 2004; Aliseda et al., 2008). Relevant in this respect is the Weber number based on the annular layer thickness, $We_a = \rho_a|U_1 - U_2|^2(R_2 - R_1)/\sigma$, where $R_2 - R_1$ represents the shear-layer thickness of the co-axial flow and $U_1 - U_2$ is given by Eq. (9) in Appendix A. For case 9, the Weber number is equal to $We_a = 89.3$, which is much higher than for case 8, see Table 2. The Weber number is also much higher than $\sqrt{\rho_a/\rho_c} = 1.05$. Marmottant and Villermaux (2004) argued that the most amplified wave length for the primary instability is then equal to $\lambda_{pi} \approx (4\pi/3)(R_2 - R_1)/\sqrt{\rho_a/\rho_c}$. For case 9, this becomes $\lambda_{pi} \approx 0.0041$ m. It should be noted here that Marmottant and Villermaux performed an inviscid analysis, neglecting the influence of viscosity on the development of the instability. Since the Ohnesorge number based on the shear-layer thickness is quite high in case 9, $Oh_a = \mu_c/\sqrt{\rho_c(R_2 - R_1)\sigma} = 6.2$, the high core viscosity will likely have a significant influence and presumably it will shift λ_{pi} to a larger value. Nevertheless, the estimated wave length of the primary instability appears to be within the range of wave lengths observed in Fig. 11.

Finally, we assess the influence of gravity for case 9. Since the instability is driven by inertial forces, the densimetric Froude number based on the annular layer thickness should actually be used instead of the Bond number based on the core radius, $Fr_a = \rho_a(U_2 - U_1)^2/(|\rho_c - \rho_a|g(R_2 - R_1))$. For case 9, this is equal to $Fr_a = 941.5$. This very high value indicates that the *direct* influence of gravity on the perturbation flow is completely negligible.

Case 10: In this case, the normalized wave number is equal to $2\pi R_1/\lambda = 0.542$ and the modified Ohnesorge number is $Oh/\sqrt{I_a} = 1.30$. Under these conditions, the flow is sensitive to a capillary-viscous instability. Eq. (1a) predicts an exponential growth rate of $\omega_i = 36.58$ s^{-1}. Although the inertial correction is significantly higher than one ($I_a = 1.17$), it appears to have negligible influence on the growth rate, since Eq. (1a) predicts $\omega_i = 36.58$ s^{-1} when $I_a = 1$ is used.

The flow might also be prone to a shear-driven instability. The Weber number based on the shear-layer thickness, is equal to $We_a = 104.6$, which is high and corresponds to the atomization regime. Based on the inviscid linear stability analysis of Marmottant and Villermaux (2004), the most amplified wave length for the primary instability is equal to $\lambda_{pi} \approx 0.015$ m, which corresponds to roughly 3 waves over the length of the periodic tube. It is expected that in the presence of a high jet viscosity, the most amplified wave length will shift to a larger value. Finally, because of the high value of We_a, Eq. (1a) should actually be modified for the presence of strong shear in the annular region, but such an analysis is beyond the scope of the present study.

Figs. 12 and 13 present the results for case 10. Clearly, the capillary instability is dominant over the shear instability, and the jet breaks up into 4 drops, as expected for a capillary instability under the given perturbation. However, the exponential growth rate is roughly twice as small as predicted. This likely originated from the presence of strong shear in the annular region (Marmottant and Villermaux, 2004; Eggers and Villermaux, 2008). Fig. 12 clearly shows the upward deflection of the wave crests by the shear flow in the annular region at $t = 0.231$ s, causing the waves to loose their initial monochromatic character.

The drops that are ultimately formed, are clearly non-spherical, being more elongated in the axial direction. This is consistent with the equilibrium perturbation amplitude in Fig. 13, which is smaller than the expected drop radius based on mass conservation and a perfectly spherical shape. To understand the origin for the deformation of the drops, we calculated the drop Bond number, $Bo_d = |\rho_c - \rho_a|gR_d^2/\sigma = 0.019$, and the drop Weber number, $We_d = \rho_a\left(U_1 - U_2\right)^2 R_d/\sigma = 57.3$, in order to assess the influence of gravity and dynamic pressure forces, respectively. From this, it is clear that gravity has a negligible influence, and that the shape deformation can be attributed to strong dynamic pressure variations along the drop from the surrounding flow. The interface curvature is highest at the bottom tip of the drops, which originated from the locally high stagnation pressure exerted by the surrounding flow on the drop.

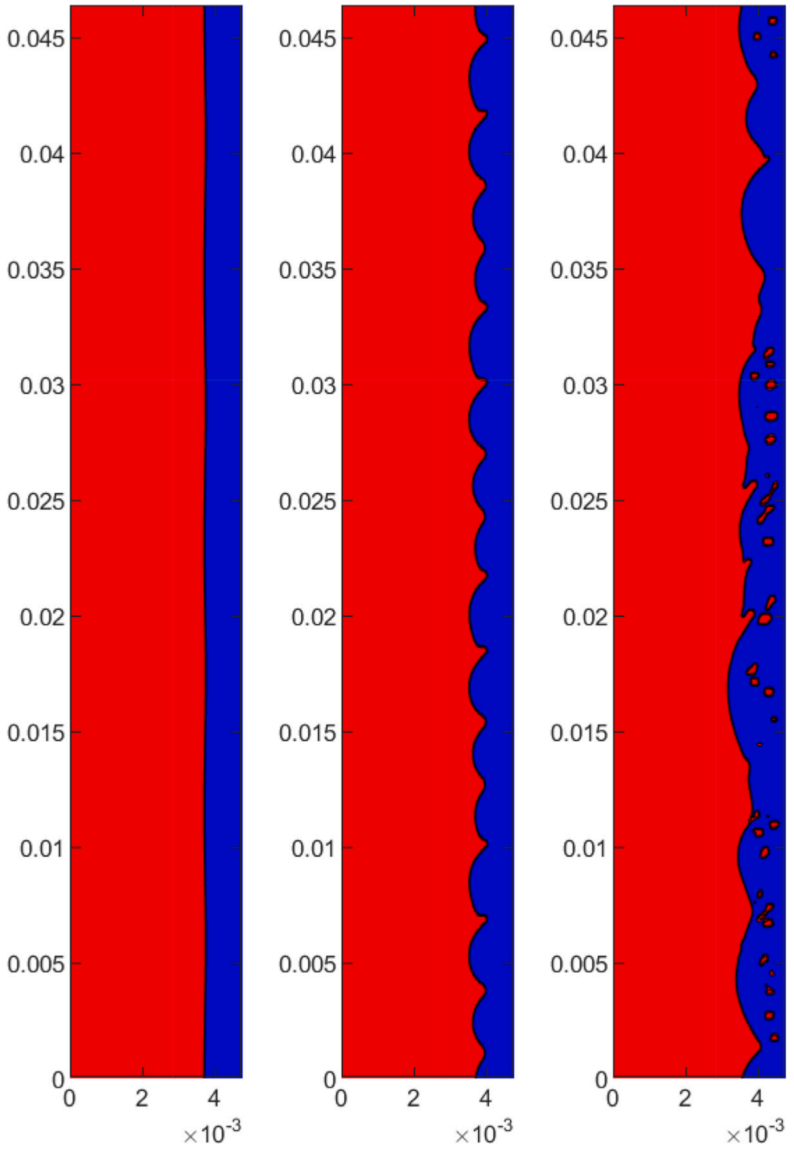

Fig. 11. Development of the flow topology for case 9 of Table 2. Left panel: $t = 0$ s. Middle panel: $t = 0.24$ s (just prior the start of droplet pinch-off). Right panel: $t = 0.98$ s.

3.3. Gravity present and non-zero pressure gradient

The previous study was repeated, but now both in the presence of gravity and a non-zero axial pressure gradient. Three cases have been simulated, see Table 3 for the parameters that have been varied. They are labeled as cases 11–13 and identical to cases 8–10 of the previous study, except for the presence of an axial pressure gradient. The latter was chosen such that the overall bulk velocity is very close to zero, see Fig. 17 in Appendix A. As can be seen from Table 3, the non-dimensional numbers derived from the flow parameters are the same as before, except for the Weber number based on the annular layer thickness. For all three cases $We_a \ll 1$, so the influence of the base flow shear in the annular region on the flow dynamics is expected to be negligible now. The comparison of cases 11–13 with cases 8–10 will thus allow us to unravel the influence of background shear of the base flow on the hydrodynamic stability of core-annular flow.

As before, the stability of the core-annular flow was tested under a sinusoidal perturbation with 4 waves over the tube length, $\lambda = l/4 =$ 0.0116 m, and a small initial perturbation amplitude, $A = 2 \cdot 10^{-5}$ m. The used grid resolution is also the same as before, $N_r \times N_z = 192 \times 768$.

Case 11: This case is similar to case 8, but with a much smaller value of We_a, so a stable flow is expected. Fig. 14 shows that this is indeed the case. The exponential decay of the initial perturbation is slower than in case 8, and slower than the predicted decay rate from Eq. (1a). The reason for this is not fully clear, but might originate from an effect of the tube wall on the perturbation flow in the annular region as $k(R_2 - R_1) = 0.56$ and is thus relatively small (Ooms, 1972). This effect of the wall is possibly stronger in the absence of background shear. Furthermore, it should be kept in mind that the initial perturbation amplitude is very small and just a factor 1.24 larger than the radial dimension of the grid cells; it cannot be excluded that the slower decay rate relates to the numerical resolution and accuracy of the methods used.

Since the flow is still prone to a capillary instability at a larger wave length of $\lambda = l$, see the discussion of case 8 in the previous section, the simulation was run for a long time to observe if any instability would develop. Interestingly, at $t \approx 5$ s, the perturbation amplitude

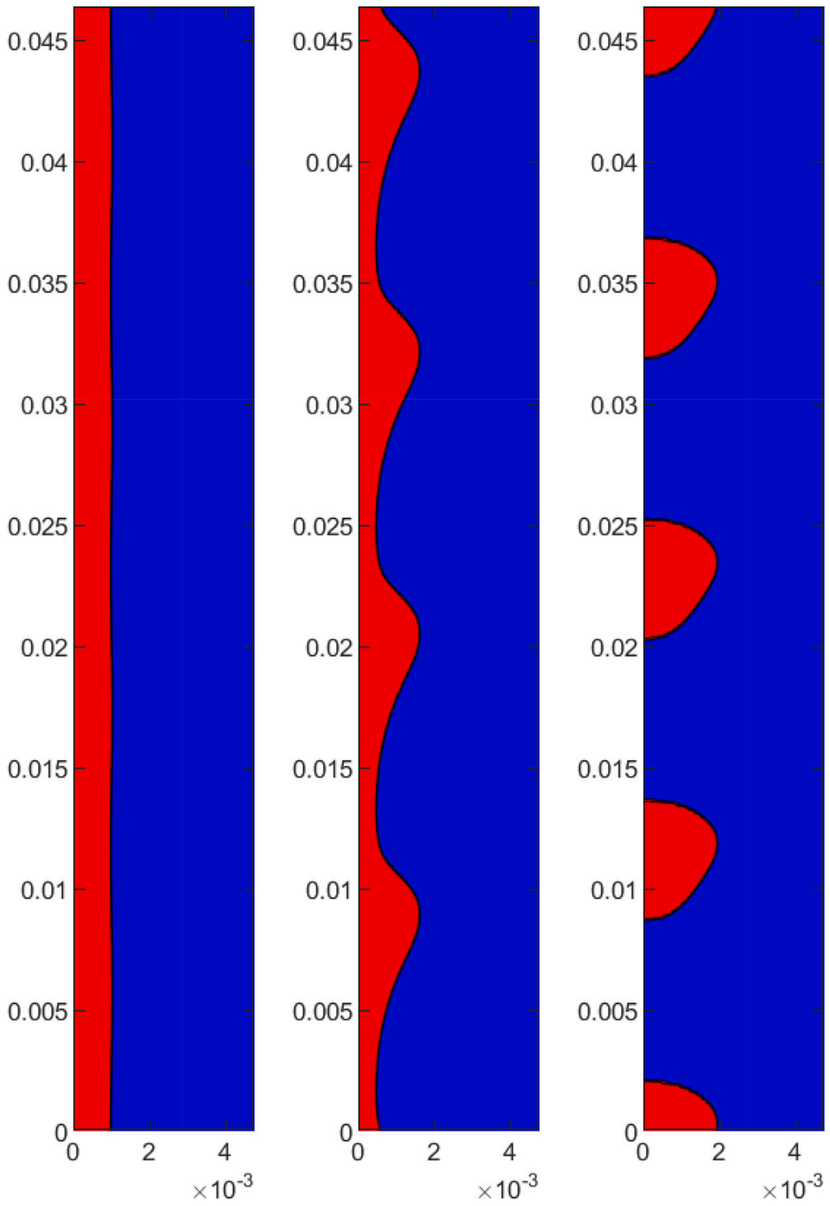

Fig. 12. Development of the flow topology for case 10 of Table 2. Left panel: t = 0 s. Middle panel: t = 0.231 s. Right panel: t = 0.46 s.

Table 3
Cases studied for a circular jet of a viscous fluid enclosed inside a narrow tube by another fluid, in the presence of gravity and a non-zero background pressure gradient. Columns 2–4 show the parameters that have been varied in the simulations: the nominal radius of the jet in the core (R1), the surface tension coefficient (σ), and the axial pressure gradient ($\partial p/\partial z$). The last 5 columns list dimensionless numbers derived from the flow parameters.

Case	R_1 (m)	σ (kg/s^2)	$\partial p/\partial z$ (Pa/m)	$2\pi R_1/\lambda$	$Oh/\sqrt{I_a}$	I_a	Bo	We_a
11	0.0037192	0.2	−9094	2.015	0.53	1.90	$6.11 \cdot 10^{-2}$	$3.21 \cdot 10^{-4}$
12	0.0037192	0.01	−9094	2.015	2.37	1.90	1.22	$6.41 \cdot 10^{-3}$
13	0.001	0.2	−9658	0.542	1.30	1.17	$4.41 \cdot 10^{-3}$	$7.76 \cdot 10^{-3}$

started to increase again at a very slow pace, until the amplitude reached a value of 10–20% of the initial perturbation amplitude. A weak oscillation in the amplitude can be observed in Fig. 14, but since the perturbation amplitude is well below the radial dimension of the grid cells, this might be a numerical artifact. It could be possibly related to discretization errors in the calculation of the interface curvature or to the diffuse representation of the interface in the numerical method. Therefore, the simulation was aborted at t = 20.5 s.

Case 12: This case is identical to case 9 in the previous section, except for a much smaller Weber number. The results are shown in Fig. 15. The nearly complete absence of background shear has a dramatic effect on the flow dynamics. The flow appears to be stable now, while in case 9 the jet was subject to atomization. In fact, the behavior of the normalized perturbation amplitude is similar to case 11. The initial instability is damped. As for case 11, the actual decay rate is slower than the predicted rate. Furthermore, after a few seconds, the perturbation amplitude increases gradually again. However, the

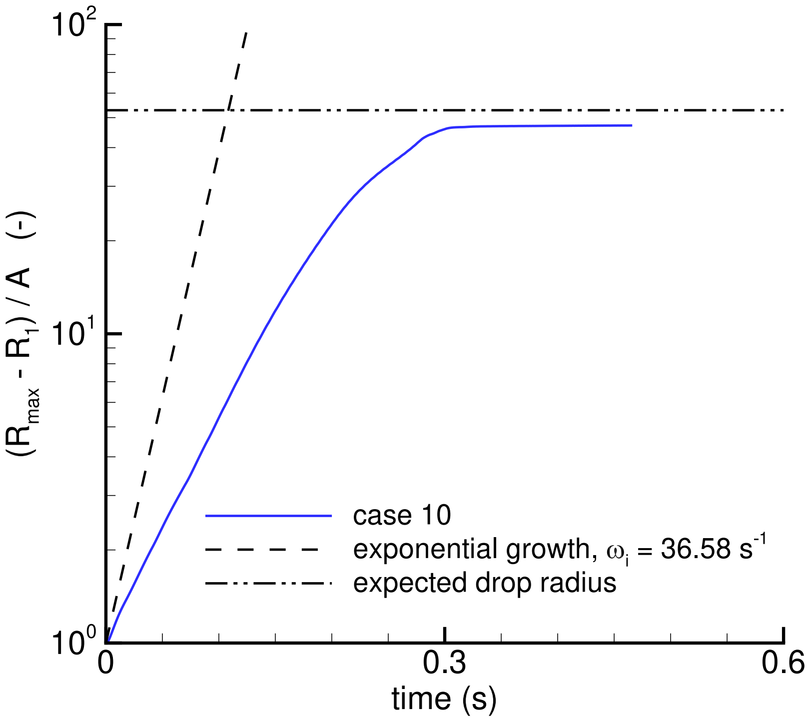

Fig. 13. Evolution of the normalized perturbation amplitude as a function of time for case 10 of Table 2. The dashed line corresponds to an exponential growth of the perturbation amplitude according to Eq. (1a). The dash-dotted line corresponds to the expected radius of the drops formed, based on mass conservation and assuming a perfectly spherical shape.

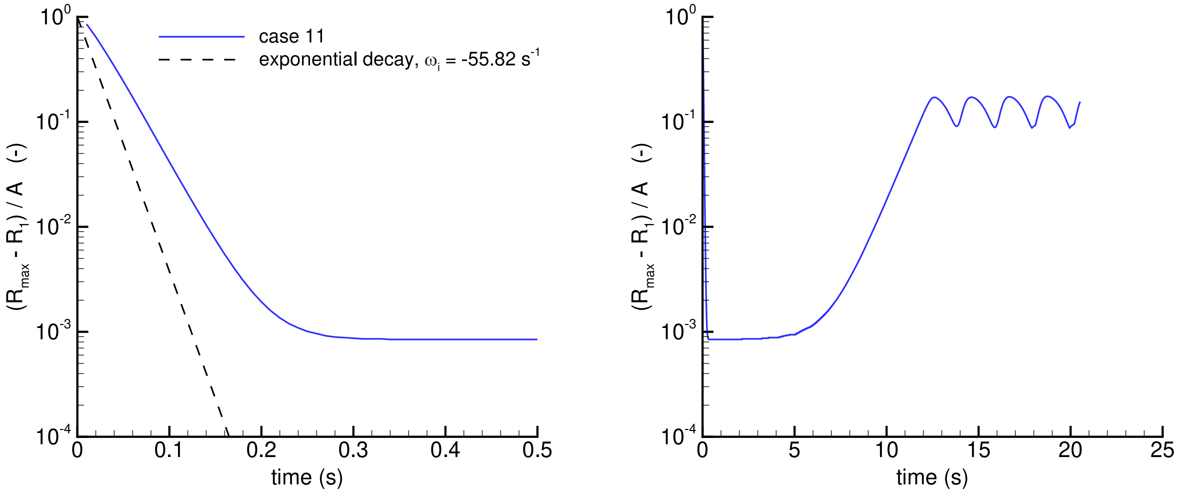

Fig. 14. Evolution of the normalized perturbation amplitude as a function of time for case 11 of Table 3. The dashed line in the left panel corresponds to an exponential decay of the perturbation amplitude according to Eq. (1a). The right panel shows the evolution over a longer time interval.

perturbation remains small and at $t \approx 135$ s, it reached an equilibrium value on the order of the initial perturbation amplitude. Therefore, it was decided to abort the simulation.

Case 13: This case is identical to case 10 in the previous section, except for a much smaller Weber number. The results are shown in Fig. 16. Similar to case 10, the flow is subject to a capillary instability. The growth rate predicted from Eq. (1a) is in fairly good agreement with the actual growth rate. This provides further evidence that the discrepancy between the predicted and observed growth rate in case 10, see Fig. 13, is caused by a dampening effect of the background shear in the annular region; this effect is not included in the dispersion relation given by Eq. (1a).

Interestingly, the jet breaks up into 4 main and 4 satellite drops, which move slowly downwards. We have not investigated the physical mechanism behind this phenomenon, or whether it relates to a grid resolution problem. Because of the presence of satellite droplets, the final perturbation amplitude is slightly smaller than the value expected for breakup into 4 perfectly spherical drops.

Another striking difference between case 13 and case 10 is the shape of the drops formed. The drops have a close to spherical shape in case 13, while in case 10 the shape is clearly non-spherical. This substantiates the influence of background shear on the drop shape, as discussed for case 10.

4. Conclusions and discussion

We have presented results from axisymmetric simulations of core-annular flow in a narrow vertical tube using the interFoam two-phase

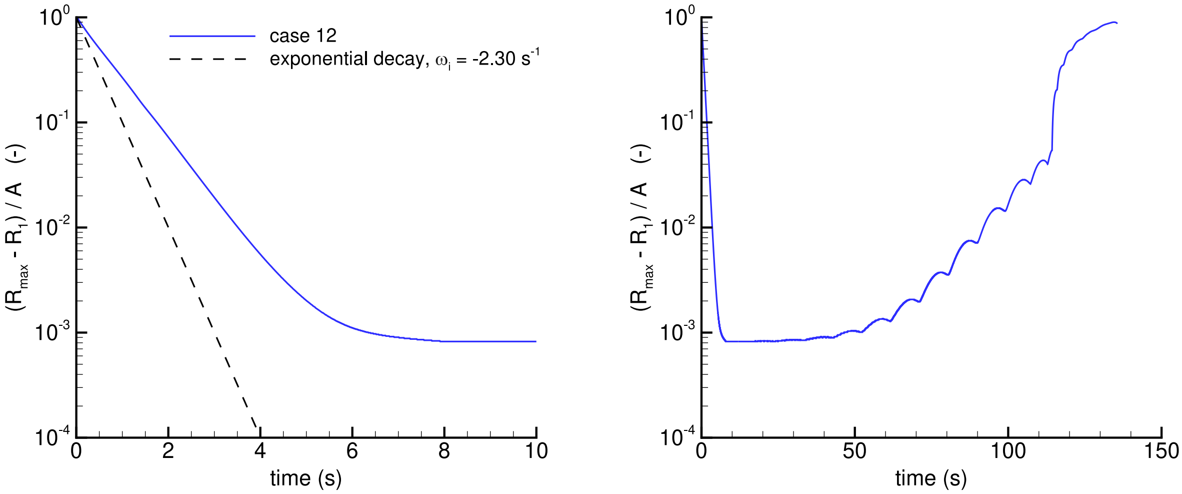

Fig. 15. Evolution of the normalized perturbation amplitude as a function of time for case 12 of Table 3. The dashed line in the left panel corresponds to an exponential decay of the perturbation amplitude according to Eq. (1a). The right panel shows the evolution over a longer time interval.

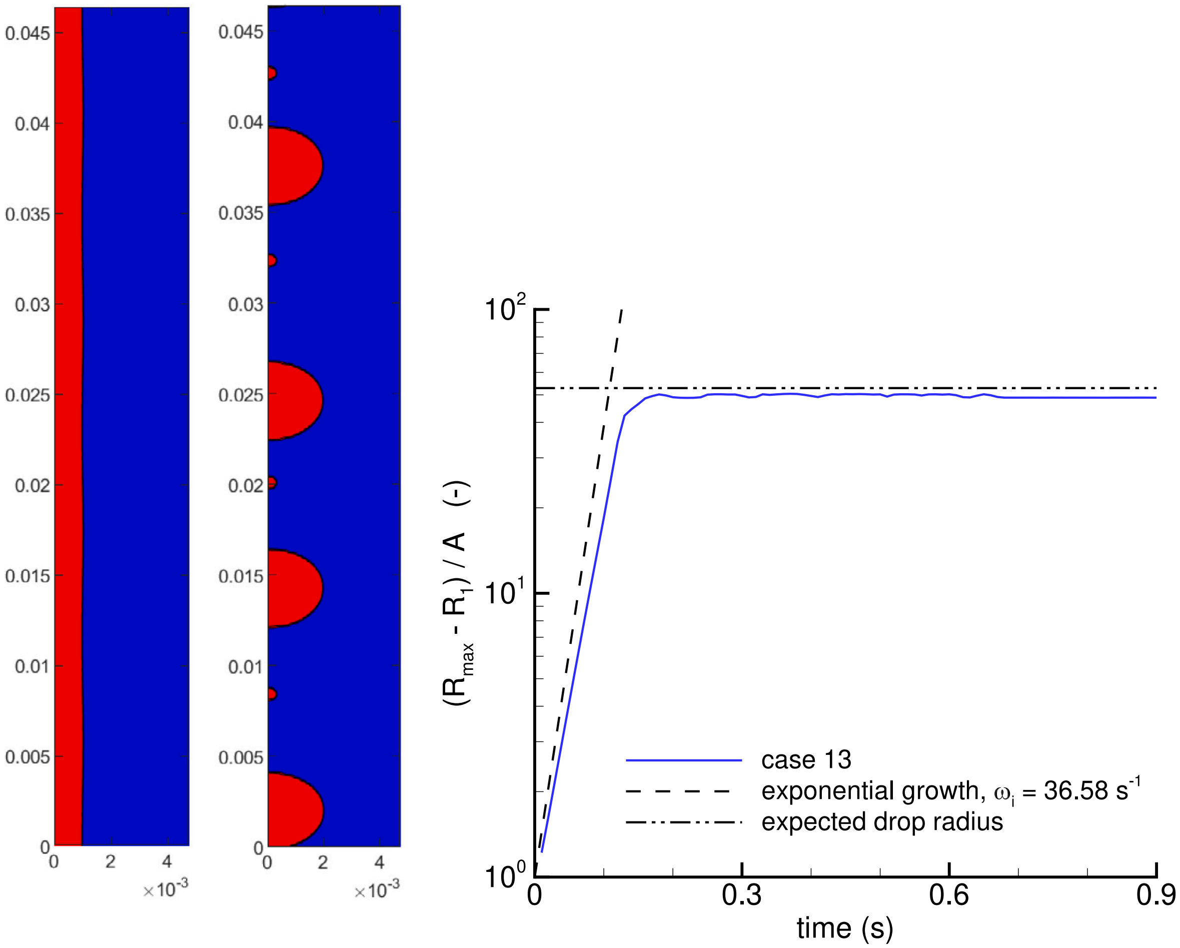

Fig. 16. Development of the flow topology for case 13 of Table 3. Left panel: t = 0 s. Middle panel: t = 1.22 s. Right panel: evolution of the normalized perturbation amplitude as a function of time. The dashed line corresponds to an exponential growth at a growth rate computed from Eq. (1a). The dash-dotted line corresponds the expected final radius of the drops.

flow solver in OpenFOAM combined with an explicit VOF method based on multicut PLIC. Special attention was paid to the grid resolution and the computational time step required for accurate results and numerical stability, respectively. The temporal hydrodynamic stability was studied for perfect core-annular flow with a high viscosity ratio between the core and the annulus under a small sinusoidal perturbation of the interface. Three different types of base flows were explored: (a) core-annular flow at rest in the absence of gravity and with a zero axial pressure gradient, (b) core-annular flow in the presence of gravity and a zero axial pressure gradient, and (c) core-annular flow close to rest in the presence of both gravity and a non-zero axial pressure gradient, which approximately cancel each other.

The simulation results were interpreted using theoretical results from linear stability analyses of thin liquid jets in free space. Simulations of type 1 were used to validate the numerical solver and to explore the influence of the flow parameters on capillary instabilities. The simulations of type 2 and type 3 provided insight in the role of background shear of the annular base flow on the hydrodynamic stability.

The main conclusions from our study are listed below:

1. The numerical solver used, is well suited for accurate simulations of flow instabilities evolving from axisymmetric, sinusoidal perturbations of the core-annular interface.
2. Provided that the length of the periodic tube is long enough, perfect core-annular flow in a narrow vertical tube is hydrodynamically unstable under certain axisymmetric, sinusoidal perturbations of the core-annular interface, either through a capillary instability or through a shear-driven instability.
3. The influence of the core viscosity and of inertial forces of the annular flow on capillary instabilities, is determined by, respectively, the Ohnesorge number, Oh, and the inertial correction factor, I_a. The inertial correction factor needs to be modified for the presence of the tube wall when $k(R_2 - R_1) \lesssim 1$.
4. The influence of background shear of the base flow in the annular region on the hydrodynamic stability, is controlled by the Weber number. For $We_a \ll 1$, the influence of shear on the hydrodynamic stability can be neglected and the flow is prone to a capillary instability when $kR_1 < 1$. For $We_a \gg 1$, the liquid jet may undergo atomization, in which small droplets are continuously pinching off from the liquid jet and entrained into the annular flow. In one specific case for which $We_a \gg 1$, still a capillary instability developed (case 9), likely because the growth under the given perturbation was sufficiently fast to prevent the onset of atomization. For this particular case, we found clear evidence of the dampening effect of shear on the growth of the capillary instability.
5. In the present study, gravity did not have a significant *direct* influence on the hydrodynamic stability of the flow, but only an *indirect* influence through the influence of gravity on the shear of the base flow. The direct influence of gravity on the perturbation flow can be assessed by evaluating the Bond number, Bo, when $We_a \ll 1$ (surface tension dominant over inertial forces), or the Froude number, $Fr_a = We_a/[\,Bo \cdot (R_2/R_1 - 1)^2\,]$, when $We_a \gg 1$ (inertial forces dominant over surface tension).

Although perfect core-annular flow is hydrodynamically unstable, it is well-known that core-annular flow with a wavy interface may be stable. Several experimental and numerical studies have confirmed this, see for instance Rodriguez and Bannwart (2006), Sotgia et al. (2008) and Li et al. (2021, 2025). It would be interesting to study the underlying physical mechanisms and the required conditions for a stable wavy pattern in more detail.

In the present study, the Weber number was either very low, $We_a \ll 1$, or very high, $We_a = O(100)$. For future research, it is recommended to study the competition between capillary and shear-driven instability mechanisms for the intermediate Weber number range. The present simulations assumed axisymmetry of the flow. While this is valid for capillary instabilities (Eggers and Villermaux, 2008), this may not be justified for shear-driven instabilities, see the discussion of case 9. Therefore, it is recommended to extend the present numerical framework to full 3D simulations for the high Weber number regime to test this. Furthermore, if the Reynolds number for the shear flow in the annular region, $Re_a = |U_1|(R_2 - R_1)/\nu_a$, is higher than the critical Reynolds number for laminar/turbulent transition, a turbulent flow should be considered (Li et al., 2025).

CRediT authorship contribution statement

Gijs Ooms: Writing – original draft, Investigation, Formal analysis, Conceptualization. **Mathieu Pourquie:** Investigation, Conceptualization. **Wim-Paul Breugem:** Writing – review & editing, Formal analysis, Conceptualization.

Declaration of competing interest

The authors declare that they have no known competing financial interests or personal relationships that could have appeared to influence the work reported in this paper.

Appendix A. Velocity profile for perfect core-annular flow

For fully-developed core-annular flow in the laminar regime, the interface between the two fluids is perfectly cylindrical and the velocity field depends only on the radial coordinate. In literature, this is commonly referred to as 'perfect core-annular flow' (PCAF) (Li et al., 2021). The PCAF velocity profile can be computed from the axisymmetric Navier–Stokes equations for an incompressible, Newtonian fluid, which in this case reduce to:

$$0 = -\frac{\partial p}{\partial z} - \rho g + \mu \frac{\partial}{\partial r}\left(r \frac{\partial u_z}{\partial r} \right) , \tag{6}$$

where z is the axial coordinate that increases in the upward direction, g is the absolute value of the gravitational acceleration, $\rho = \rho_c$ and $\mu = \mu_c$ for $r < R_1$, and $\rho = \rho_a$ and $\mu = \mu_a$ for $r > R_1$.

The axial pressure gradient is a constant, independent of the axial and radial coordinate. The flow is subject to a no-slip condition at the tube wall. At the centerline, the radial velocity gradient is zero because of symmetry. Furthermore, the velocity and the viscous shear stress are continuous across the interface at $r = R_1$. Using these boundary conditions, Eq. (6) can be solved for $u_z(r)$. The solution is given by:

$$u_z(r) = \begin{cases} \frac{f_c}{4\mu_c}\left(R_1^2 - r^2\right) + \frac{f_a}{4\mu_a}\left(R_2^2 - R_1^2\right) + \frac{(\rho_a - \rho_c) g R_1^2}{2\mu_a} \ln\left(\frac{R_2}{R_1}\right) & , \quad r \le R_1 , \\ \frac{f_a}{4\mu_a}\left(R_2^2 - r^2\right) + \frac{(\rho_a - \rho_c) g R_1^2}{2\mu_a} \ln\left(\frac{R_2}{r}\right) & , \quad R_1 \le r \le R_2 , \end{cases} \tag{7}$$

where $f_c = -\partial p/\partial z - \rho_c g$ and $f_a = -\partial p/\partial z - \rho_a g$ have been introduced for ease of notation.

From the velocity profile, the following bulk (area-averaged) velocities can be obtained for the core and the annular region:

$$U_1 = \frac{f_c R_1^2}{8\mu_c} + \frac{f_a}{4\mu_a}\left(R_2^2 - R_1^2\right) + \frac{(\rho_a - \rho_c) g R_1^2}{2\mu_a} \ln\left(\frac{R_2}{R_1}\right) , \tag{8a}$$

$$U_2 = \frac{f_a (R_2^2 - R_1^2)}{8\mu_a} + \frac{(\rho_a - \rho_c) g R_1^2}{2\mu_a} \left[\frac{1}{2} - \frac{R_1^2 \ln\left(\frac{R_2}{R_1}\right)}{R_2^2 - R_1^2} \right] . \tag{8b}$$

Finally, the difference in bulk velocities can be used to estimate the degree of shear in the flow. This is given by:

$$U_1 - U_2 = \frac{f_c R_1^2}{8\mu_c} + \frac{f_a (R_2^2 - R_1^2)}{8\mu_a} + \tag{9}$$

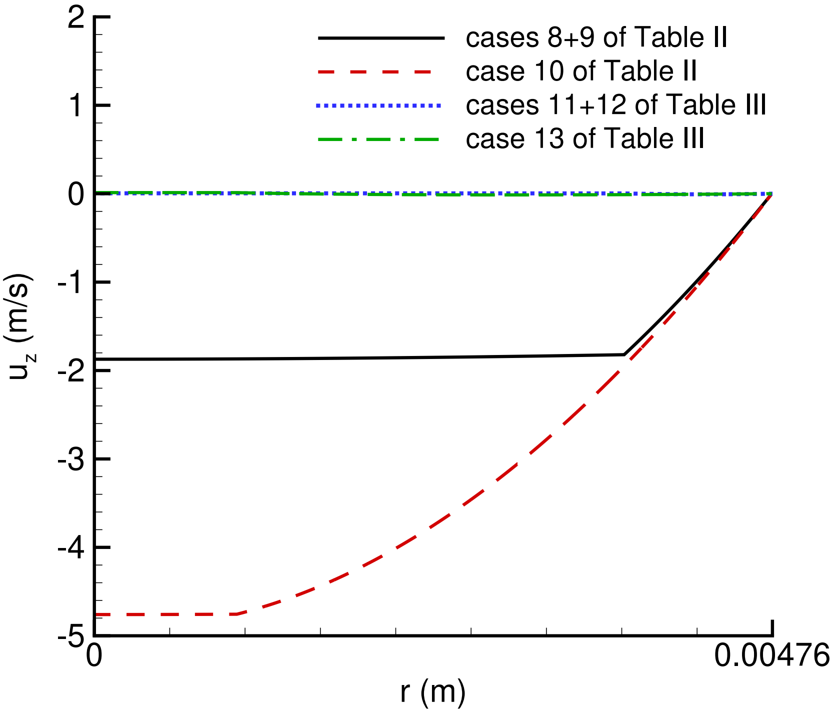

Fig. 17. PCAF velocity profiles of the cases listed in Tables 2 and 3.

$$\frac{(\rho_a-\rho_c)gR_1^2}{2\mu_a}\left[\frac{R_2^2}{R_2^2-R_1^2}\ln\left(\frac{R_2}{R_1}\right)-\frac{1}{2}\right].$$

The PCAF velocity profiles of the cases listed in Tables 2 and 3, are shown in Fig. 17. Due to the high viscosity of the core compared to the annular region, the velocity profile in the core is nearly uniform. For cases 8–10 of Table 2, the velocity profile is approximately parabolic in the annular region, given by the first term on the right-hand side of the expression for the annular region in Eq. (7). For cases 11–13 of Table 3, the velocity is close to zero everywhere, because in these cases the upward force from the imposed axial pressure gradient was chosen to approximately balance the downward gravitational force.

Appendix B. Capillary-inertial time step constraint for numerical stability

It is assumed here that the time step constraint from surface tension for numerical stability is set by the requirement that capillary-inertial waves traveling along the jet interface with a wave length of $\lambda = 2\Delta x$, are resolved in time. This will suppress the strength of parasitic currents that originate from the discrete representation of the jet interface, see the discussion in Deshpande et al. (2012). Based on a linear stability analysis, the angular frequency of the waves, ω_r, is given by the following expression (Eggers and Villermaux, 2008):

$$\omega_r = \frac{1}{\sqrt{2}}\frac{1}{\tau_I}\sqrt{\frac{(kR_1)^4-(kR_1)^2}{1+\frac{1}{2}\left(\frac{\rho_a}{\rho_c}\right)(kR_1)^2\ln\left(1+\frac{1}{kR_1}\right)}}\quad \text{for}\quad kR_1 \geq 1\,, \tag{10}$$

where the denominator in the square root is a correction for inertial effects from the fluid in the annular region. Assuming that $kR_1 \gg 1$, this equation can be simplified according to:

$$\omega_r \approx \frac{1}{\sqrt{2}}\frac{1}{\tau_I}\frac{(kR_1)^2}{\sqrt{1+\frac{1}{2}\left(\frac{\rho_a}{\rho_c}\right)kR_1}}\quad \text{for}\quad kR_1 \gg 1\,. \tag{11}$$

From this, the capillary-inertial time step constraint was estimated according to $\Delta t_{\max}^{\mathrm{cap}} = 0.5\cdot\pi/\omega_r$, equivalent to Eq. (59) in Brackbill et al. (1992). Furthermore, since $\Delta r < \Delta x$ in almost all simulations, Δx was replaced by $\Delta r = R_2/N_r$ with N_r the number of grid cells over the tube radius. The final expression used to estimate the capillary-inertial time step constraint is given by:

$$\Delta t_{\max}^{\mathrm{cap}} = \frac{1}{\sqrt{2}\,\pi N_r^2}\sqrt{\frac{R_2}{R_1}}\sqrt{1+\left(\frac{\pi N_r}{2}\right)\left(\frac{\rho_a}{\rho_c}\right)\left(\frac{R_1}{R_2}\right)}\sqrt{\frac{\rho_c R_2^3}{\sigma}}\,. \tag{12}$$

This stability criterion holds specifically for core-annular flow. Brackbill et al. (1992) derived a different criterion, which does not contain flow-specific parameters. To ease the comparison with our criterion, their generic criterion is rewritten into the following form:

$$\Delta t_{\max}^{\mathrm{BB}} = \frac{1}{2\sqrt{\pi}N_r^{3/2}}\sqrt{1+\frac{\rho_a}{\rho_c}}\sqrt{\frac{\rho_c R_2^3}{\sigma}}\,, \tag{13}$$

where we replaced Δx by $\Delta r = R_2/N_r$ as before.

For $\left(\frac{\pi N_r}{2}\right)\left(\frac{\rho_a}{\rho_c}\right)\left(\frac{R_1}{R_2}\right) \ll 1$, as in case 1 of Table 1, our criterion scales approximately with $1/N_r^2$, while the criterion of Brackbill et al. scales with $1/N_r^{3/2}$. This originates from the different dispersion relations used for estimating the angular frequency of the capillary waves: the dispersion relation for a cylindrical jet in our case versus the dispersion relation for a planar interface between two semi-infinite media in their case. For case 1 of Table 1, $\Delta t_{\max}^{\mathrm{cap}} = 1.36\cdot 10^{-6}$ s based on our criterion and $\Delta t_{\max}^{\mathrm{BB}} = 1.05\cdot 10^{-5}$ s based on their criterion. Thus, our criterion yields a nearly 8 times smaller time step in this case.

For $\left(\frac{\pi N_r}{2}\right)\left(\frac{\rho_a}{\rho_c}\right)\left(\frac{R_1}{R_2}\right) \gg 1$, as in case 8 of Table 2, Eq. (12) can be simplified to:

$$\Delta t_{\max}^{\mathrm{cap}} \approx \frac{1}{2\sqrt{\pi}\,N_r^{3/2}}\sqrt{\frac{\rho_a R_2^3}{\sigma}}\quad \text{for}\quad \left(\frac{\pi N_r}{2}\right)\left(\frac{\rho_a}{\rho_c}\right)\left(\frac{R_1}{R_2}\right) \gg 1\,. \tag{14}$$

Note that in this limit our time step does not depend on the density and the radius of the core anymore. Also, similar to the criterion of

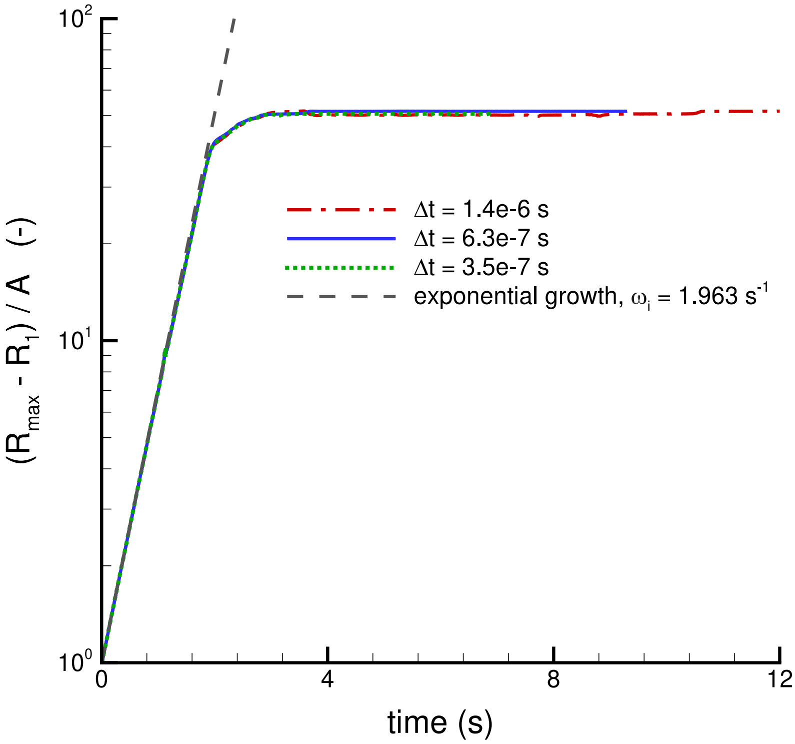

Fig. 18. Evolution of the normalized perturbation amplitude, $(R_{\max}(t) - R_1)/A$, as a function of time for case 1 of Table 1 at a fixed grid resolution of $N_r \times N_z = 128 \times 128$. Here, $R_{\max}$ is the maximum jet radius, R_1 is the nominal jet radius, and A is the initial perturbation amplitude. The lines represent different computational time steps as indicated in the legend. Also shown is the line corresponding to exponential growth at a growth rate computed from Eq. (3).

Brackbill et al. the time step now scales with $1/N_r^{3/2}$. For case 8 of Table 2, $\Delta t^{\mathrm{cap}}_{\max} = 2.45 \cdot 10^{-6}$ s based on either Eq. (12) or (14), and $\Delta t^{\mathrm{BB}}_{\max} = 3.39 \cdot 10^{-6}$ s based on the criterion of Brackbill et al. Thus, our time step is approximately a factor 1.4 times smaller in this case.

Appendix C. Evaluation of time step criterion

Fig. 18 shows the influence of the computational time step on the temporal evolution of the normalized perturbation amplitude for case 1 of Table 1 at a fixed grid resolution of $N_r \times N_z = 128 \times 128$. Notice that the sensitivity study was performed with a coarser grid than indicated in the table in order to reduce the computational load. The maximum allowed time step for numerical stability was limited by the criterion for surface tension, see Eq. (4). The largest time step investigated, $\Delta t = 1.4 \cdot 10^{-6}$ s, was computed from this criterion with the prefactor equal to $\alpha = 0.463$. The other two time steps examined, are a factor 2.22 and a 4 times smaller, respectively.

The profiles for the three different time steps nearly collapse; only very small differences are observed at large times, after the jet has been broken up into a single drop in this case, see Fig. 2. The initial growth of the perturbation amplitude is in very good agreement with the prediction from linear stability analysis given by Eq. (3), which indicates that the flow was sufficiently resolved in both space and time. Our time step criterion for surface tension thus appears to be sufficient to maintain a numerically stable solution.

Appendix D. Grid convergence study

A grid convergence study was performed for case 1 of Table 1. Three different grid resolutions, $N_r \times N_z$, were tested: 128×128, 192×192, and 256×256. The computational time step was determined from Eq. (4) and equal to, respectively, $\Delta t = 1.4 \cdot 10^{-6}$ s, $\Delta t = 6.3 \cdot 10^{-7}$ s and $\Delta t = 3.5 \cdot 10^{-7}$ s. Fig. 19 shows the results for the temporal evolution of the normalized perturbation amplitude.

During the early development, the perturbation amplitude is growing exponentially. The growth rate is in excellent agreement with the prediction from Eq. (3). The lines for different grid resolutions collapse with each other during the early stage. However, small differences between the lines become visible close to breakup of the jet at $t \approx 2$ s and at later times when a droplet has been formed. The results for the highest two resolutions are close to each other and appear to be somewhat more accurate than the results for the 128×128 grid. In particular, for the 128×128 grid, the final perturbation amplitude slightly underestimates the expected drop radius based on mass conservation for the core liquid, suggesting that the drop is not fully spherical in this case. This is also substantiated by Fig. 20, which shows the location of the minimum jet radius (wave trough) over time.

For the 128×128 grid, the final drop exhibits a slight downward offset and the edges of the drop in the axial direction are separated slightly more than one drop diameter from each other. The results for the highest two grid resolutions are again close to each other. No offset is observed in the location of the final drop and the distance between the minima is very close to the expected drop diameter. Based on these results, the 192×192 grid appears to be optimal to achieve the desired numerical accuracy at an acceptable computational load.

Data availability

The OpenFOAM case files and videos of selected cases showing the flow development are openly available in 4TU. ResearchData repository at https://doi.org/10.4121/b28e9ad3-e1fc-499b-ab1c-9c78f18a75e1.

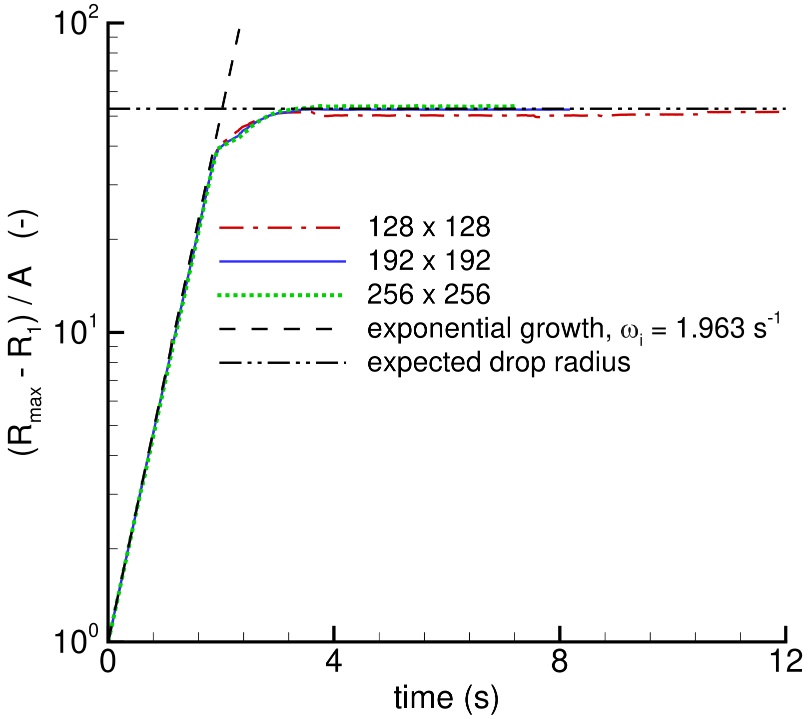

Fig. 19. Temporal evolution of the normalized perturbation amplitude, $(R_{\text{max}}(t) - R_1)/A$, for case 1 of Table 1. The lines represent different grid resolutions, $N_r \times N_z$, as indicated in the legend. For the corresponding values of the computational time steps, see the main text. Also shown is the line corresponding to exponential growth at a growth rate computed from Eq. (3), and the line corresponding to the expected tip of the final droplet.

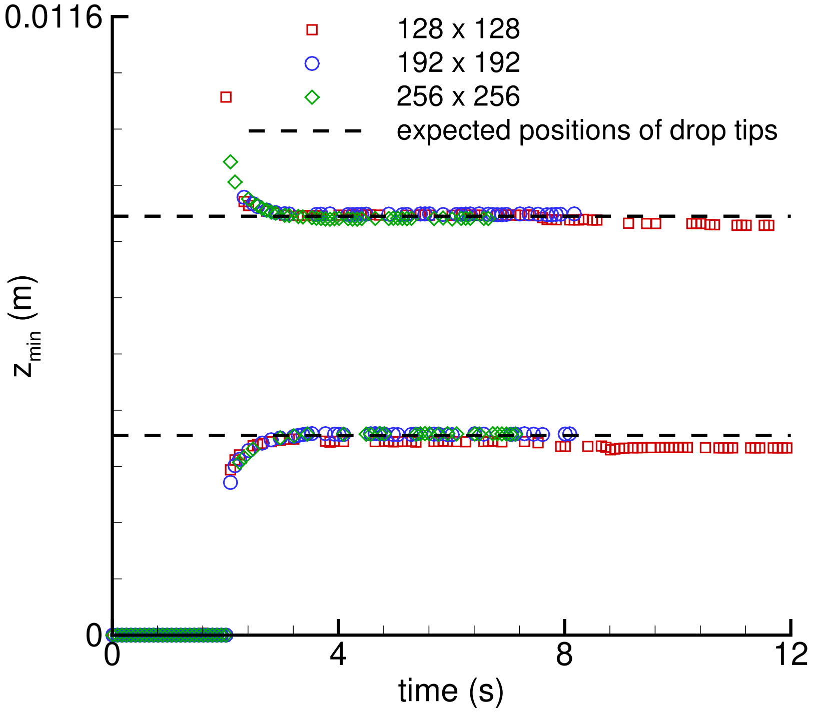

Fig. 20. Temporal evolution of the position of minimum jet radius, $z_{\text{min}} = z(R_{\text{min}})$, for case 1 of Table 1. The simulation data was sampled every 0.08 s. Symbols represent different grid resolutions, $N_r \times N_z$, as indicated in the legend. For the corresponding time steps, see the main text. The dashed lines indicate the expected locations of the axial tips of the final drop formed after breakup of the jet.

References

Aliseda, A., Hopfinger, E.J., Lasheras, J.C., Kremer, D.M., Berchielli, A., Connolly, E.K., 2008. Atomization of viscous and non-Newtonian liquids by a coaxial high-speed gas jet. Experiments and droplet size modeling. Int. J. Multiph. Flow 34 (2), 161–175.

Brackbill, J.U., Kothe, D.B., Zemach, C., 1992. A continuum method for modeling surface tension. J. Comput. Phys. 100 (2), 335–354.

Deshpande, S., Ammolu, L., Trujillo, M., 2012. Evaluating the performance of the two-phase flow solver interfoam. Comput. Sci. Discov. 5, 014016, 2012.

Eggers, J., Villermaux, E., 2008. Physics of liquid jets. Rep. Progr. Phys. 71, 036601.

Guillot, P., Colin, A., Utada, A.S., Ajdari, A., 2007. Stability of a jet in confined pressure-driven byphasic flows at low Reynolds numbers. Phys. Rev. Lett. 99, 104502.

Housz, E.M.R.M. Ingen, Ooms, G., Henkes, R.A.W.M., Pourquie, M.J.B.M., Kidess, A., Radhakrishnan, R., 2017. A comparison between numerical predictions and experimental results for horizontal core-annular flow with a turbulent annulus. Int. J. Multiph. Flow 95, 271–282.

Joseph, D.D., Bai, R., Chen, K.P., 1997. Core-annular flows. Annu. Rev. Fluid Mech. 29, 65–90.

J.S. Piña, D. Godino, Corzo, S., Ramajo, D., 2022. Air injection in vertical water column: Experimental test and numerical simulation using volume of fluid and two-fluid methods. Chem. Eng. Sci. 255, 117665.

Lamb, H., 1881. On the oscillations of a viscous spheroid. Proceedings of the London Mathematical Society, vol. s1-13, no. 1, pp. 51–70.

Li, H., 2023. Waves and turbulence in core-annular pipe flow (Ph.D. thesis). Delft University of Technology.

Li, H., M.J.B.M. Pourquié, G. Ooms, Henkes, R.A.W.M., 2021. Simulation of turbulent horizontal oil-water core-annular flow with a low-Reynolds number k–ϵ model. Int. J. Multiph. Flow 142, 103744.

Li, H., M.J.B.M. Pourquié, G. Ooms, Henkes, R.A.W.M., 2025. Simulation of interfacial waves in core-annular pipe flow with a turbulent annulus. J. Fluids Eng. 147, 1–12, 021401.

Li, J., Renardy, Y., 1999. Direct simulation of unsteady axisymmetric core-annular flow with a high viscosity ratio. J. Fluid Mech. 391, 123–149.

Marmottant, P., Villermaux, E., 2004. On spray formation. J. Fluid Mech. 498, 73–111.

Ooms, G., 1972. The hydrodynamic stability of core-annular flow of two ideal liquids. Appl. Sci. Res. 26, 147–158.

Ooms, G., Poesio, P., 2003. Stationary core-annular flow through a horizontal pipe. Phys. Rev. E 68, 066301.

Ooms, G., Pourquie, M.J.B.M., 2024. Two-dimensional numerical analysis of waves at the interface of laminar core-annular flow in a vertical pipe: detailed investigation of influence of several physical parameters. Pet. Sci. Eng. 8 (1), 7–15.

Ooms, G., Pourquie, M., Beerens, J.C., 2013. On the levitation force in horizontal core-annular flow with a large viscosity ratio and small density ratio. Phys. Fluids 25, 032102.

Plateau, J.A.F., 1873. Statique expérimentale et théorique des liquides soumis aux seules forces moléculaires., vol. 2, Gauthier-Villars..

Rayleigh, Lord, 1879. On the capillary phenomena of jets. Proc. Roy. Soc. 29, 71–97.

Rodriguez, O.M.H., Bannwart, A.C., 2006. Experimental study on interfacial waves in vertical core flow. j. Pet. Sci. Eng. 54, 140–148.

Rykner, M., Saikali, F., Bruneton, A., Mathieu, B., Nikolayev, V.S., 2024. Plateau–Rayleigh instability in a capillary: assessing the importance of inertia. J. Fluid. Mech. 1001, A15.

Sotgia, G., Tartarini, P., Stalio, E., 2008. Experimental analysis of flow regimes and pressure drop reduction in oil–water mixtures. Int. J. Multiph. Flow 34, 1161–1174.

Sweby, P.K., 1984. High resolution schemes using flux limiters for hyperbolic conservation laws. SIAM J. Numer. Anal. 21 (5), 995–1011.

Tripathi, S., Tabor, R.F., Singh, R., Bhattacharya, A., 2017. Characterization of interfacial waves and pressure drop in horizontal oil-water core-annular flow. Phys. Fluids 29, 002109.

Weller, H.G., Tabor, G., Jasak, H., Fureby, C., 1998. A tensorial approach to computational continuum mechanics using object-oriented techniques. Comput. Phys. 12 (6), 620–631.

Xie, B., Jiang, F., Lin, H., Zhang, M., Gui, Z., Xiang, J., 2023. Review of core-annular flow. Energies 16 (3), 1496.